Cell

Structural basis for VIPP1 oligomerization and maintenance of thylakoid membrane integrity

Graphical abstract

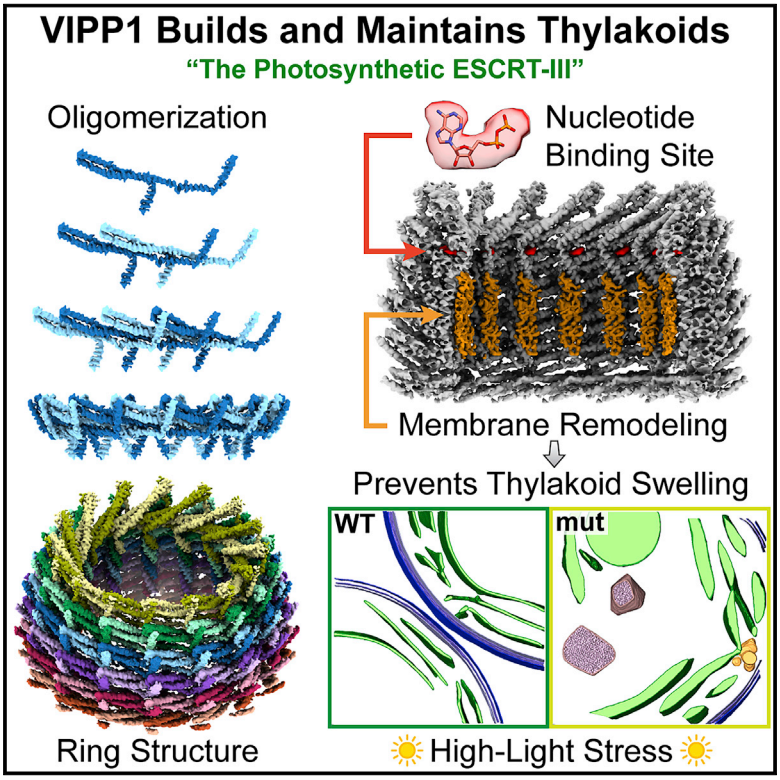

Authors

Tilak Kumar Gupta, Sven Klumpe, Karin Gries, ..., Jan M. Schuller, Michael Schroda, Benjamin D. Engel

Correspondence

jan.schuller@synmikro.uni-marburg.de (J.M.S.), schroda@bio.uni-kl.de (M.S.), ben.engel@helmholtz-muenchen.de (B.D.E.)

In brief

Structure-function analysis and *in situ* visualization of VIPP1 provide insights into how this ESCRT-III homolog manipulates membranes to support thylakoid biogenesis and maintenance in cyanobacteria, algae, and plants.

Highlights

- Cryo-EM reveals how VIPP1 oligomerizes, hydrolyzes nucleotides, and binds lipids
- Lipid binding by VIPP1's H1 helix maintains thylakoid integrity under high-light stress
- VIPP1 coats mediate contact between thylakoids and the chloroplast envelope
- VIPP1 is the photosynthetic homolog of ESCRT-III membrane-remodeling proteins

Gupta et al., 2021, Cell *184*, 3643–3659
July 8, 2021
https://doi.org/10.1016/j.cell.2021.05.011

CellPress

Cell

CellPress

Article

Structural basis for VIPP1 oligomerization and maintenance of thylakoid membrane integrity

Tilak Kumar Gupta,[1,11] Sven Klumpe,[1,11] Karin Gries,[2,11] Steffen Heinz,[3,11] Wojciech Wietrzynski,[1,4,11] Norikazu Ohnishi,[5] Justus Niemeyer,[2] Benjamin Spaniol,[2] Miroslava Schaffer,[1] Anna Rast,[1,3] Matthias Ostermeier,[3] Mike Strauss,[6] Jürgen M. Plitzko,[1] Wolfgang Baumeister,[1] Till Rudack,[7,8] Wataru Sakamoto,[5] Jörg Nickelsen,[3] Jan M. Schuller,[9,*] Michael Schroda,[2,*] and Benjamin D. Engel[1,4,10,12,*]

[1]Department of Molecular Structural Biology, Max Planck Institute of Biochemistry, 82152 Martinsried, Germany
[2]Molecular Biotechnology and Systems Biology, Technische Universität Kaiserslautern, 67663 Kaiserslautern, Germany
[3]Department of Molecular Plant Sciences, LMU Munich, 82152 Martinsried, Germany
[4]Helmholtz Pioneer Campus, Helmholtz Zentrum München, 85764 Neuherberg, Germany
[5]Institute of Plant Science and Resources, Okayama University, Kurashiki, Okayama 710-0046, Japan
[6]Department of Anatomy and Cell Biology, McGill University, Montreal, QC H3A 17C, Canada
[7]Biospectroscopy, Center for Protein Diagnostics (PRODI), Ruhr University Bochum, 44801 Bochum, Germany
[8]Department of Biophysics, Faculty of Biology & Biotechnology, Ruhr University Bochum, 44780 Bochum, Germany
[9]SYNMIKRO Research Center and Department of Chemistry, Philipps-University Marburg, 35032 Marburg, Germany
[10]Department of Chemistry, Technical University of Munich, 85748 Garching, Germany
[11]These authors contributed equally
[12]Lead contact
*Correspondence: jan.schuller@synmikro.uni-marburg.de (J.M.S.), schroda@bio.uni-kl.de (M.S.), ben.engel@helmholtz-muenchen.de (B.D.E.)
https://doi.org/10.1016/j.cell.2021.05.011

SUMMARY

Vesicle-inducing protein in plastids 1 (VIPP1) is essential for the biogenesis and maintenance of thylakoid membranes, which transform light into life. However, it is unknown how VIPP1 performs its vital membrane-remodeling functions. Here, we use cryo-electron microscopy to determine structures of cyanobacterial VIPP1 rings, revealing how VIPP1 monomers flex and interweave to form basket-like assemblies of different symmetries. Three VIPP1 monomers together coordinate a non-canonical nucleotide binding pocket on one end of the ring. Inside the ring's lumen, amphipathic helices from each monomer align to form large hydrophobic columns, enabling VIPP1 to bind and curve membranes. *In vivo* mutations in these hydrophobic surfaces cause extreme thylakoid swelling under high light, indicating an essential role of VIPP1 lipid binding in resisting stress-induced damage. Using cryo-correlative light and electron microscopy (cryo-CLEM), we observe oligomeric VIPP1 coats encapsulating membrane tubules within the *Chlamydomonas* chloroplast. Our work provides a structural foundation for understanding how VIPP1 directs thylakoid biogenesis and maintenance.

INTRODUCTION

Thylakoid membranes orchestrate the light-dependent reactions of oxygenic photosynthesis, splitting water to generate Earth's oxygen and using the electrons and H^+ liberated from this reaction to produce NADPH and ATP. These bioenergetic molecules are then used to remove CO_2 from the atmosphere and convert it into the sugar that feeds Earth's heterotrophic life. Thus, most of the energy flowing through our planet's complex web of life originates in the intricate thylakoid membranes of plants, algae, and cyanobacteria.

Despite the central importance of thylakoids to our biosphere, we know very little about how these sheet-like membranes are constructed or how their integrity is maintained under environmental stress. Vesicle-inducing protein in plastids 1 (VIPP1, also known as IM30) co-evolved with thylakoids and is believed to play a key role in thylakoid biogenesis and homeostasis (Li et al., 1994; Vothknecht et al., 2012). Complete knockout of VIPP1 blocks thylakoid assembly and is lethal (Zhang et al., 2012). Reduction of VIPP1 expression in the cyanobacterium *Synechocystis* sp. PCC6803 (Westphal et al., 2001; Fuhrmann et al., 2009b), the cyanobacterium *Synechococcus* sp. PCC7002 (Zhang et al., 2014), the eukaryotic green alga *Chlamydomonas reinhardtii* (Nordhues et al., 2012), and the vascular plant *Arabidopsis thaliana* (Kroll et al., 2001; Aseeva et al., 2007) strongly impairs the biogenesis of thylakoid membranes, resulting in lower levels of the membrane-embedded photosystems and a corresponding drop in photosynthetic activity. VIPP1 knockdown has also been observed to cause dramatic thylakoid swelling in *Arabidopsis* and *Chlamydomonas* exposed to high

light (Nordhues et al., 2012; Zhang et al., 2012), indicating that VIPP1 helps thylakoids cope with acute stress. In support of this function, overexpression of VIPP1 improves recovery of *Arabidopsis* from heat stress (Zhang et al., 2016).

In vitro, VIPP1 self-assembles into large homo-oligomers of variable symmetry: *Synechocystis* VIPP1 (*syn*VIPP1) and *Arabidopsis* VIPP1 (*at*VIPP1) primarily form rings (Aseeva et al., 2004; Fuhrmann et al., 2009a; Zhang et al., 2016; Saur et al., 2017), whereas *Chlamydomonas* VIPP1 (*cr*VIPP1) and its paralog VIPP2 make long helical rods (Liu et al., 2007; Theis et al., 2019, 2020). Higher-order VIPP1 oligomers may also form *in vivo*. In *Arabidopsis*, VIPP1-GFP accumulates in puncta and larger filament-like structures (Aseeva et al., 2004; Zhang et al., 2012, 2016). In *Synechocystis* and *Synechococcus*, VIPP1-GFP also forms puncta, which vary in abundance and mobility in response to changing light conditions (Bryan et al., 2014; Gutu et al., 2018). VIPP1 has no predicted transmembrane domains, but it has a strong affinity for lipids *in vitro* and *in vivo* that is mediated by its N-terminal amphipathic helix (Li et al., 1994; Kroll et al., 2001; Otters et al., 2013; McDonald et al., 2017). *In vitro*, *syn*VIPP1 rings have been shown to bind liposomes and induce fusion (Hennig et al., 2015), and *cr*VIPP1 rods have been observed to encapsulate liposomes (Theis et al., 2019). Adding to the enigmatic complexity of VIPP1 function, *at*VIPP1 and *syn*VIPP1 were recently reported to have GTPase activity, but VIPP1 lacks a canonical guanosine triphosphate (GTP)-binding domain (Ohnishi et al., 2018; Junglas et al., 2020b).

RESULTS

High-resolution model of VIPP1 oligomerization

A mechanistic understanding of the many described functions of VIPP1 requires high-resolution structural information. To date, the only available 3D structures of VIPP1 are negative-stain electron microscopy (EM) densities that lack the resolution to discern individual VIPP1 monomers (i.e., protomers) (Saur et al., 2017). Therefore, we determined structures of heterologously expressed *syn*VIPP1 rings by single particle cryo-electron microscopy (cryo-EM). Iterative classification and refinement of ~337,000 particles from 8,120 images yielded five different cryo-EM density maps corresponding to VIPP1 rings with C14, C15, C16, C17, and C18 rotational symmetries (Figures 1H and S1A–S1D) at resolutions ranging from 3.8–5.0 Å (Figures S1E and S1F). Using a combination of homology modeling, *ab initio* structure prediction, and refinement by molecular dynamics flexible fitting (MDFF), we built atomic models of the two <4 Å structures (C15 and C16) and then extended the model building to cover all five symmetries (Figure S1G).

The oligomeric structure of the *syn*VIPP1 ring resembles a tightly interwoven basket (Figures 1A–1C; Video S1). Contrary to a previous model that positions the VIPP1 monomers vertically, parallel to the ring's central axis (Saur et al., 2017), the monomers are arranged horizontally into stacked layers (Figures 1D and 1E). Six layers are resolved in C14–C16, whereas C17 and C18 contain seven layers. The rings are tapered on both ends, with a smaller diameter at the top (layer 1) than at the bottom (layer 6 or 7) (Figure S1K). The VIPP1 protein is predicted to contain seven α helices (H1–H7) (Figure 1F; Otters et al., 2013; Zhang et al., 2016). Our density maps resolve five α helices, with the predicted H4 and H5 domains forming a single helix, which we named H4/5 to maintain nomenclature consistent with previous studies (Figure 1G). The N-terminal H1 domains of each layer align with each other to form vertical columns that face the lumen of the ring (Figure 1C). H2 and H3 make a coiled-coil hairpin that is connected to H4/5 by a loop of seven amino acids (Figure 1G). H6 protrudes on the outer surface of the ring (Figures 1B and S1H–S1J). Within a layer, H3 and H4/5 together extend to pass behind two neighboring monomers, and then H6 points upward and binds the H2/H3 hairpin of the third neighboring monomer, forming the interwoven structure (Figures 1D and 1E). In addition, the luminal H1 columns stabilize the ring from the inside and help hold the stacked layers together. In total, each VIPP1 monomer can interact with up to 16 other monomers from three layers (Figure S2).

H7 was unresolved in our density maps, presumably because of flexibility. This small C-terminal helix with a predicted amphipathic structure is connected to H6 by an intrinsically disordered linker of ~32 amino acids. Based on the position of H6 on the outer wall of the ring, it is clear that H7 extends outside of the ring. Thus, one can envision the complete VIPP1 ring as a "hairy basket" decorated with many flexible H7 domains. This structure is consistent with the dispensability of H7 for VIPP1 oligomerization (Liu et al., 2007; Otters et al., 2013; Hennig et al., 2017) and ideally positions H7 to interact with external factors in the cellular environment, such as membranes or chaperones, which may regulate VIPP1 dynamics (Liu et al., 2005; Liu et al., 2007; Zhang et al., 2016). H1–H6 are homologous to bacterial phage shock protein A (PspA) (Westphal et al., 2001; Otters et al., 2013), which also forms an oligomeric ring (Hankamer et al., 2004), and heterologous expression of VIPP1 can functionally complement deletion of PspA in *Escherichia coli* (DeLisa et al., 2004; Zhang et al., 2012). However, PspA cannot compensate for VIPP1 deficiency (Zhang et al., 2016), underscoring the thylakoid-specific role of H7.

Comparing our five *syn*VIPP1 structures (Figures 1H and S1G) revealed four regions of flexibility in the VIPP1 monomer (F1–F4) that allow it to build tapered rings of different symmetries (Figure 1I). All four regions bend and flex to enable monomers to assemble into the different layers of a ring (Figures 1J and S1L; Video S2). In contrast, for the same layer across the symmetries (e.g., layer 3 in C14–C18), the flexibility primarily comes from region F3 (Figures 1K and S1M; Video S2). This loop apparently enables *syn*VIPP1 rings to expand to reach higher symmetries with increased diameter.

VIPP1 rings assemble a tripartite nucleotide-binding pocket

To check whether unmodeled density was present, we calculated difference maps between the cryo-EM densities and the VIPP1 molecular models (Figures 2 and 3). We observed a small difference density between layers 1 and 2 (Figures 2A and 2B) that could accommodate the structure of a bound nucleotide (Figure 2C). Comparison with nucleotide densities from other cryo-EM structures (Banerjee et al., 2016) showed a better

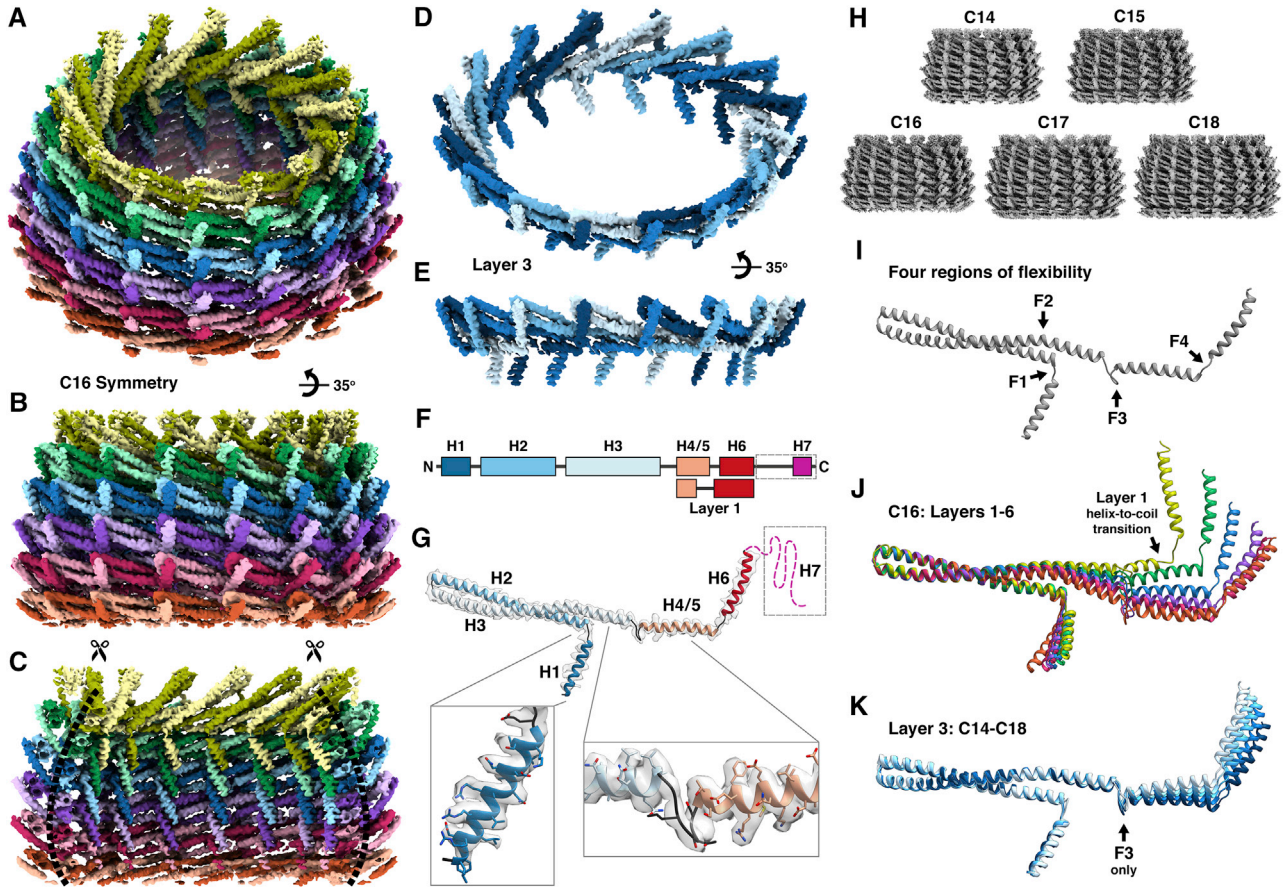

Figure 1. VIPP1 monomers interweave and flex to form basket-like ring structures

(A and B) Inclined (A) and side (B) views of the cryo-EM density map for a *syn*VIPP1 ring with C16 symmetry. The ring consists of six layers shown in different colors (layer 1, olive green; layer 6, orange). Two shades of each color highlight the interwoven structure.

(C) Cut-open view of the ring reveals how the H1 helices of each monomer align to form vertical columns that face toward the lumen.

(D and E) Inclined (D) and side (E) views of layer 3, shown in isolation to visualize the way VIPP1 monomers (in four shades of blue) extend and interact.

(F and G) Schematic of the VIPP1 monomer's secondary structure elements (F; α helices H1–H7, colored rectangles) and the corresponding regions on the VIPP1 molecular model, fit into the EM density (G; transparent white). The C-terminal domain (dashed line box), which includes H7, was not resolved in the EM density map, likely because of high flexibility. Magnified views of two regions of the monomer structure (H1 and the loop connecting H3 with H4/5) show the fit of the VIPP1 model into the EM density map.

(H) Cryo-EM density maps for *syn*VIPP1 rings with five symmetries (C14–C18).

(I) Comparing the molecular models of these structures (Figure S1G) revealed four regions of flexibility in the VIPP1 monomer (F1–F4).

(J) Superposition of the VIPP1 monomers from each layer of the C16 ring. F1–F4 all flex to assemble the ring. The C-terminal side of H4/5 is remodeled into a coil in layer 1 (Figure S3B–S3D).

(K) Superposition of the VIPP1 monomers from layer 3 of each symmetry (C14, darkest blue; C18, lightest blues). Only the F3 loop flexes to accommodate different ring symmetries.

See also Figures S1 and S2 and Videos S1 and S2.

match with ADP than the larger density of ATPγS (Figure S3A). To confirm the presence of nucleotide in the *syn*VIPP1 structure, we subjected the purified protein to reverse-phase ion-pair high-performance liquid chromatography (RPIP-HPLC) coupled to electrospray ionization mass spectroscopy (ESI-MS). We detected a molecular mass corresponding to ADP (Figures S4A and S4B) that, we reasoned, might come from the ATP wash performed during protein purification. When we sequentially washed with ATP followed by GTP, we detected ADP and GDP in the purified VIPP1 rings (Figure 2F), indicating that VIPP1 may be able to bind and hydrolyze both ATP and GTP.

The VIPP1 nucleotide binding site is formed by bringing together different regions of three VIPP1 monomers, two from layer 1 and one from layer 2 (Figure 2C). The nucleotide is accommodated by flexibility in region F4 of layer 1, with the C-terminal portion of H4/5 opening into a short coil (Figures 1J and S3B–S3D). We fit an ADP molecule into the EM density and refined the molecular model by interactive MDFF (Goh et al., 2016), revealing characteristic structural and charge distribution features of a nucleotide binding pocket (Figures 2D, 2E, S3E, and S3F). In our refined model, Lys133 and Arg44 from layer 2 use their positive charges to clamp the phosphates of

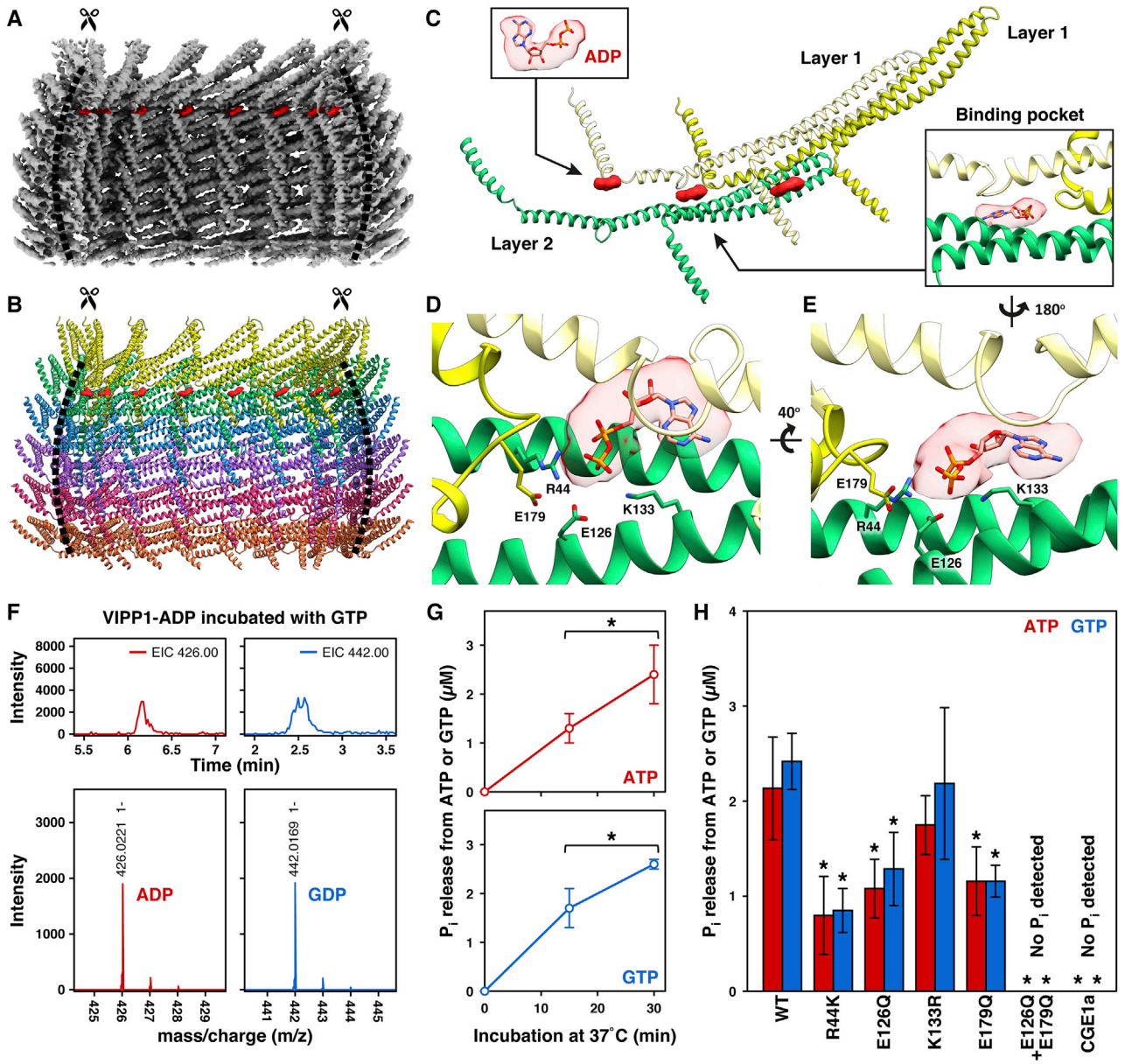

Figure 2. Nucleotide binding sites are formed at the interface between three VIPP1 monomers

(A and B) Cut-open side views of the C16 cryo-EM density map (A) and molecular model (B), with extra EM densities shown in red.

(C) The extra densities and three VIPP1 monomers extracted from the model of the complete ring (layer 1, yellow; layer 2, green). Insets show fitting of the ADP structure into the extra density (top left) and a nucleotide binding pocket formed at the interface between three monomers (bottom right).

(D and E) Close-up views of the nucleotide binding pocket from the top (D) and side (E). Side chains and labels are displayed for residues predicted by the model to position the nucleotide and coordinate nucleophilic attack on the γ-phosphate (Figure S3F).

(F) RPIP-HPLC profiles (top panels) and subsequent ESI-MS (bottom panels) of wild-type (WT) *syn*VIPP1 following incubation with GTP. Some of the bound ADP (Figures S4A and S4B) was exchanged for GDP.

(G) *In vitro* nucleotide hydrolysis assays showing that WT *syn*VIPP1 causes phosphate release from ATP and GTP. Error bars, standard deviation from 3–4 replicates. Asterisks indicate a significant change between time points (*$p < 0.05$, Welch's t test).

(H) *In vitro* ATP and GTP hydrolysis by WT *syn*VIPP1 compared with mutations in the nucleotide binding pocket (the double mutant is indicated with a "+"). CGE1a was used as a negative control. This nucleotide exchange factor of chloroplast Hsp70 does not possess ATPase activity and was purified using the same protocol as for VIPP1. Error bars, standard deviation from 6–10 replicates. Asterisks indicate a significant change compared with the WT (*$p < 0.05$, Welch's t test).

See also Figures S3 and S4.

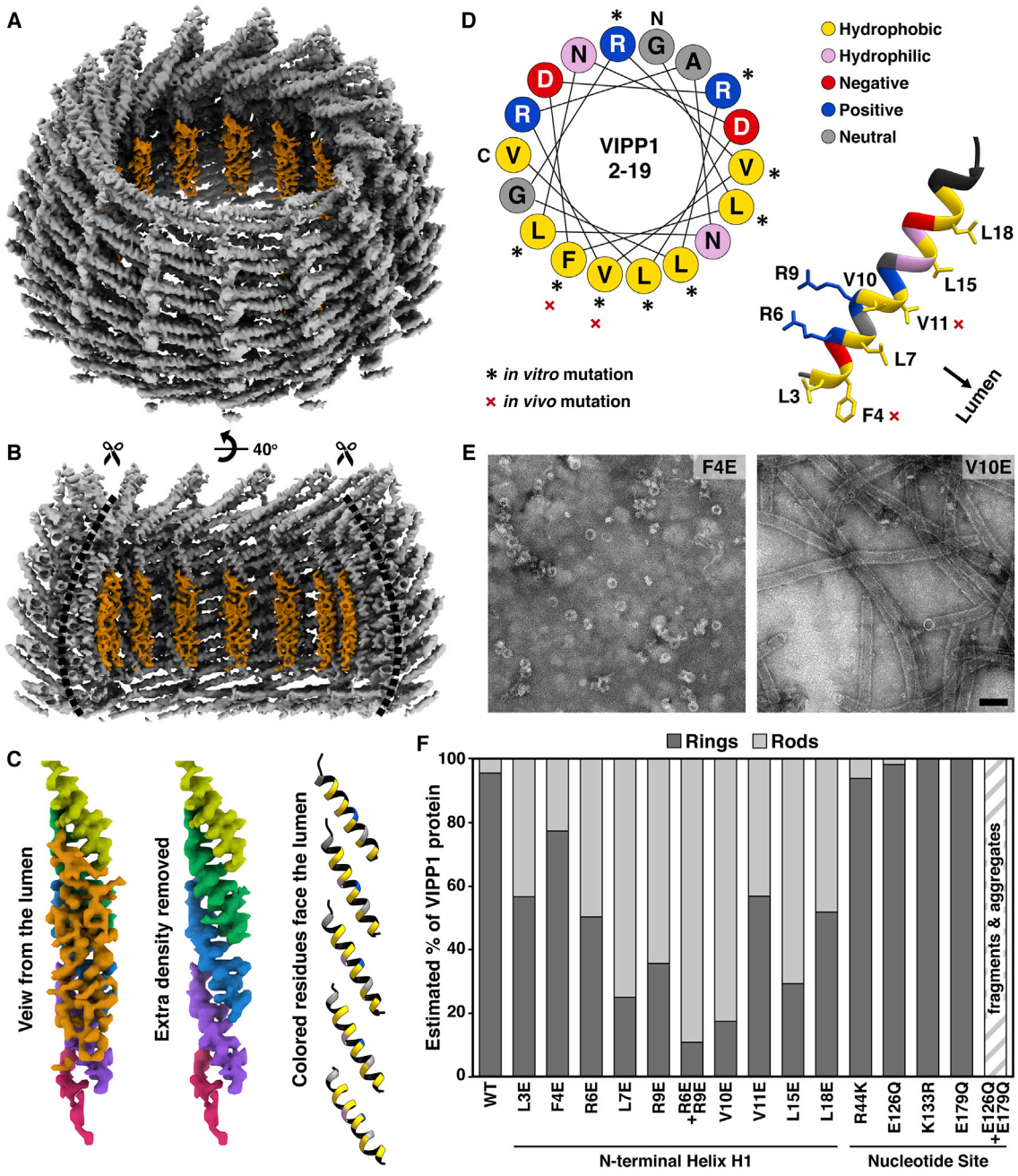

Figure 3. Columns of H1 helices form large hydrophobic surfaces on the luminal face of the VIPP1 ring

(A and B) Inclined (A) and side (B) views of the C15 cryo-EM density map, with extra EM densities shown in orange.

(C) Luminal view of a column of N-terminal H1 helices, shown as EM density (colored by layer according to Figure 1; left column with orange extra density, center column with extra density removed) and as a molecular model (right column, only the lumen-facing residues are colored according to D). Yellow hydrophobic residues face the ring lumen. Helix H1 of layer 5 (magenta) is poorly resolved because of flexible interactions with the unanchored and, thus, unresolved H1 of layer 6.

(D) Helical wheel plot of residues 2–19 (left) and corresponding molecular model (right), showing the amphipathic structure of H1. *In vitro* mutations (examined here and in Figure S4E) are indicated by an asterisk and shown with labeled side chains on the molecular model. *In vivo* mutations (examined in Figures 4, 5, S6, and S7) are indicated by a red "x."

(E and F) Example negative-stain EM images for two *in vitro* mutant proteins (E) and the estimated percentage of protein assembled into rings or rods (F). See Figure S5 for negative-stain EM of all *in vitro* mutants in this study, including the nucleotide pocket mutants from Figure 2.

Scale bar: 100 nm.

the nucleotide. Glu126 from layer 2 and Glu179 on the opened coil of layer 1 are well positioned to orient a water molecule for nucleophilic attack on the γ-phosphate (Figures S3E and S3F). When the nucleotide densities from the C15, C16, and C17 rings were viewed at a lower threshold, each displayed a small additional density that could correspond to Mg^{2+} (Figure S3A), a standard feature of NTPase pockets that helps coordinate the nucleotide. VIPP1 lacks one common element of ATP and GTP binding sites, the Walker A (ATPases) or P loop (GTPases) motif (Walker et al., 1982). However, there is no universal fingerprint for nucleotide binding, and other known NTPases also lack this motif (Saraste et al., 1990).

We next performed *in vitro* nucleotide hydrolysis assays and observed that purified *syn*VIPP1 and *cr*VIPP1 can hydrolyze ATP and GTP (Figures 2G, S4C, and S4D), consistent with previous reports of GTPase activity in *syn*VIPP1, *at*VIPP1, and PspA (Ohnishi et al., 2018; Junglas et al., 2020b). Single amino acid substitutions in *syn*VIPP1 Arg44, Glu126, and Glu179 (R44K, E126Q, E179Q) reduced phosphate release from ATP and GTP (Figure 2H), supporting our structural model of the nucleotide binding pocket. Double mutation of Glu126 and Glu179 (E126Q+E179Q) abolished phosphate release, further corroborating that these residues coordinate hydrolysis. Mutation of Lys133 to Arg (K133R) did not have a significant effect. However, residue 133 is an Arg in *cr*VIPP1 and PspA, possibly explaining the tolerance of the *syn*VIPP1 nucleotide pocket for K133R substitution. Although all *syn*VIPP1 proteins with single mutations in the nucleotide pocket produced ring structures, the E126Q+E179Q double mutant did not assemble into rings or rods, instead forming fragments and disorganized aggregates (Figure S5). Therefore, we conclude that nucleotide hydrolysis appears to be required for *in vitro* oligomerization of *syn*VIPP1 into ring structures.

Structural basis for VIPP1 lipid binding

A second difference density not accounted for by VIPP1 monomers was found in the lumen of the ring specifically along the H1 columns (Figures 3A–3C). Previous studies have determined that H1 is required for lipid binding (Otters et al., 2013; McDonald et al., 2015, 2017), and our structure clearly reveals the mechanism of this interaction. H1 is an amphipathic helix that orients its hydrophilic side toward the VIPP1 ring wall and its hydrophobic side toward the lumen (Figure 3D). As a result, the H1 columns form large hydrophobic surfaces on the inside of the VIPP1 ring (Figure 3C). These hydrophobic H1 columns explain how liposomes are drawn into *cr*VIPP1 rods (Theis et al., 2019) and how *syn*VIPP1 rings can mediate liposome fusion (Hennig et al., 2015). The extra density seen along the H1 columns is likely endogenous lipid, which is commonly co-purified with VIPP1 and PspA from *E. coli* cells (Standar et al., 2008; Otters et al., 2013).

We made structure-directed mutations to the H1 hydrophobic interface as well as to Arg residues proposed to impart specificity to negatively charged lipids (McDonald et al., 2015, 2017; Figure 3D). To our surprise, all of these H1 mutations caused *syn*VIPP1 to form more rod structures (Figures 3E, 3F, and S5). Thus, binding of H1 to lipids may influence how VIPP1 oligomeric assemblies form, tuning the equilibrium between rings and rods (see Discussion). Interestingly, several H1 mutations also showed reduced phosphate release from ATP and GTP (Figure S4E), indicating a potential allosteric effect between lipid binding and nucleotide hydrolysis.

VIPP1 lipid interaction protects thylakoids under high-light stress

Based on our high-resolution structure, we made *in vivo* mutations in two conserved H1 residues previously shown to mediate lipid binding in PspA (F4E and V11E) (Jovanovic et al., 2014; McDonald et al., 2017) and then examined the effects on thylakoid architecture in native cells using cryo-focused ion beam (cryo-FIB) milling followed by *in situ* cryo-electron tomography (cryo-ET) (Asano et al., 2016; Rast et al., 2019). In low light (30 μmol photons $m^{-2}s^{-1}$), both mutants grew slower than a wild-type (WT) control strain (Figures 4A, S6A, and S6B). In high light (200 μmol photons $m^{-2}s^{-1}$), the growth rate of F4E decreased, and V11E failed to grow at all. To test the acute effects of high-light stress, liquid cell cultures were grown to log phase in low light and then transferred to high light for 24 h. VIPP1 levels were reduced in both mutant strains compared with the WT (Figures 4B and S6C–S6F), indicating that VIPP1 may be destabilized *in vivo* when lipid binding is impaired. However, upon shifting to high light, the mutant and WT strains all showed a similar ~2-fold increase in VIPP1 protein levels (Figure 4B). Levels of the photosynthetic proteins D1, Rieske, and PsaD (subunits of photosystem II, cytochrome b_6f, and photosystem I, respectively) were comparable between the mutants and WT in low light but up to 40% reduced in both mutants under high light (Figures S6C–S6F). In contrast, the thylakoid curvature-inducing protein CurT was only marginally reduced in the mutants under high light.

In WT cells, thylakoid architecture remained relatively unchanged in high light, with thylakoid lumen width expanding mildly from ~6.5 to ~9 nm (Figures 4C–4E and 4L; Video S3). Both mutant strains showed a moderate degree of thylakoid swelling in low light, but when shifted to high light, they both experienced extreme swelling (~16 to ~47 nm in F4E and ~12 to ~34 nm in V11E) (Figures 4F–4L; Video S3). The severity of thylakoid swelling varied between individual cells (Figures 4F, 4I and S6G). As thylakoids swell, high curvature is maintained at thylakoid tips, presumably by the CurT protein (Heinz et al., 2016). Under prolonged stress, the tip curvature is lost, resulting in formation of large round vesicles covered in membrane-bound ribosomes and phycobilisomes, markers of their thylakoid origin. Although both mutants experience dramatic thylakoid swelling (Figure 4L), it is interesting that F4E survives high light exposure better than V11E (Figure 4A) despite lower VIPP1 protein levels (Figure 4B). This result underscores the importance of Val11, which is centrally positioned on the H1 hydrophobic surface (Figure 3D).

In low and high light, both mutants exhibited aberrant membrane structures at the thylakoid convergence zones, regions that have been implicated in thylakoid biogenesis (Stengel et al., 2012; Rast et al., 2015). Instead of the high-curvature convergence membranes that contact the plasma membrane (Figures 4D and 4E; Rast et al., 2019), we observed clusters of round membranes that appeared to contain cytosolic material

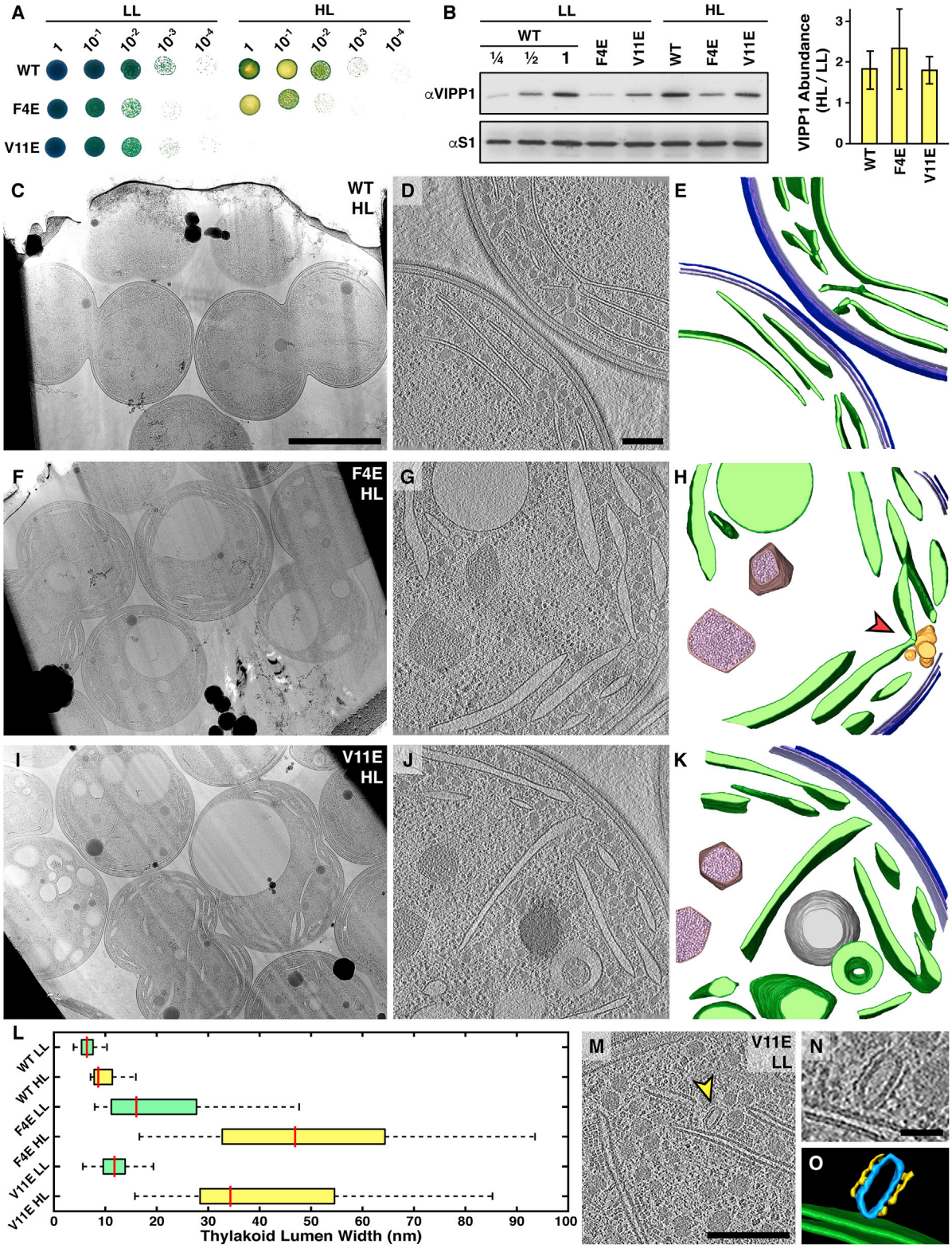

Figure 4. VIPP1 lipid interaction maintains thylakoid architecture under high-light stress

(A) Spot growth tests of WT (control, where endogenous *vipp1* was replaced by the wild-type gene with an upstream kanamycin resistance cassette at the same position as for the mutants), F4E, and V11E strains after 5 days on agar plates in low light (LL; 30 μmol photons $m^{-2}s^{-1}$) and high light (HL; 200 μmol photons $m^{-2}s^{-1}$). Agar plates are displayed with more natural contrast in Figures S6A and S6B.

(legend continued on next page)

(Figures 4G, 4H, and S7). Similar aberrant membranes have been observed at the thylakoid convergence zones of *Chlamydomonas* VIPP1 knockdown cells (Nordhues et al., 2012), indicating an evolutionarily conserved function.

VIPP1 forms membrane-encapsulating oligomers *in situ*

Careful inspection of the *Synechocystis* tomograms also revealed structures in close perpendicular contact with thylakoid membranes that resembled membranes encapsulated by a protein coat (Figures 4M–4O and 5A–5H). *In situ* structural measurements of the protein coat diameter and membrane-protein distance were consistent with *in vitro syn*VIPP1 rings and *cr*VIPP1 rods (Figures 5I and 5J). However, we also observed these coated membrane structures in some tomograms of the F4E and V11E mutants, where VIPP1 lipid binding is impaired. Therefore, if these encapsulated membranes are indeed coated by VIPP1, then the F4E and V11E substitutions may not completely ablate lipid interactions, which would be consistent with their milder phenotypes compared with the lethal VIPP1 knockout. To explore the possibility that these *in situ* membrane coats contain VIPP1, we next performed cryo-ET of *Synechocystis* cells expressing VIPP1-GFP from the endogenous locus (Figure S8; Bryan et al., 2014). In our best-aligned tomograms, we could resolve an extra layer of density decorating the outside of the protein coat (Figures S8A–S8D). The spacing of this extra density is consistent with GFP attached to the end of the flexible H7 domain plus seven additional linker residues that were added to this fusion protein (Figures S8E and S8F). Therefore, we conclude that the thylakoid-associated encapsulated membranes we observe *in situ* may be coated by VIPP1. Interestingly, these putative *syn*VIPP1 structures appear to respond to high-light stress, as we observed a ~3-fold reduction in their abundance after shifting cells from low to high light (Figure S8G).

Despite the putative GFP density we observed decorating the *Synechocystis* structures (Figure S8), the VIPP1-GFP fluorescence signal was not sufficient to enable direct correlation with cryo-ET. Because of limitations in the resolution of fluorescence microscopy and the precision of targeting by FIB milling, cryo-correlative light and EM (cryo-CLEM) is currently best suited for cellular regions spanning at least 200–500 nm that contain strong fluorescent signal (Bäuerlein et al., 2017; Wilfling et al., 2020; Klein et al., 2021). To perform reliable cryo-CLEM of VIPP1 structures *in situ*, we used a *Chlamydomonas* strain overexpressing VIPP1-mCherry that exhibited abundant bright fluorescent puncta (Figure 6). Accurate correlation was guided by the VIPP1-mCherry signal and cellular features, including starch granules and cell boundaries (Figures 6A–6D and 6H–6K). Cryo-ET of the correlated positions revealed the VIPP1-mCherry puncta to be clusters of membrane tubules coated in VIPP1 protein (Figures 6E–6G, 6L, and 6M; Videos S4 and S5). Detailed inspection of these *in situ* VIPP1 structures clearly showed that VIPP1 can oligomerize into helical assemblies inside the native chloroplast (Figures 6O–6R). The *in situ* VIPP1 structures varied in helical pitch and handedness (Figures 6Q and 6S), similar to what we observed previously with *in vitro* VIPP1 rods (Figure 6N; Theis et al., 2019). However, *in situ* VIPP1 membrane coats exhibited an even wider range of pitches and sometimes appeared disorganized (Figures 6P and 6T), perhaps reflecting a more dynamic nature. Intriguingly, we also observed a VIPP1 coat mediating a membrane continuity between converging thylakoid membranes and the chloroplast envelope (Figures 6T–6V; Video S6).

Our cryo-CLEM study definitively shows that *cr*VIPP1 can form rod-like helical assemblies that encapsulate tubular membranes within the native chloroplast. Comparison of our *in vitro syn*VIPP1 ring structures (Figure 1) with a concurrent cryo-EM structure of a helical PspA rod (Junglas et al., 2021 [this issue of *Cell*]) reveals that VIPP1/PspA rings and rods share the same fold and oligomerize through very similar interactions. Therefore, we conclude that the molecular insights revealed by our high-resolution structures of *syn*VIPP1 rings are likely relevant to the variety of VIPP1 ring and rod architectures that assemble *in vitro* and *in vivo*.

DISCUSSION

VIPP1 and PspA share structural and functional homology with ESCRT-III

The oligomer-forming helices of VIPP1 (H1–H6) are closely conserved with PspA. Therefore, the structural mechanisms revealed in our study are relevant to PspA's role in maintaining plasma membrane integrity, which underlies bacterial pathogenesis and antibiotic resistance (Darwin, 2013; Manganelli and Gennaro, 2017). In addition to PspA, VIPP1 also shares structural homology with ESCRT-III proteins (in particular, CHMP1B), which oligomerize in a similar fashion by using flexible "hinge" loops to interweave their extended α helices, forming helical assemblies of variable symmetry that bind and curve membranes (McCullough et al., 2015; Nguyen et al., 2020). This structural conservation is detailed more extensively in two

(B) Western blot analysis of VIPP1 protein levels in liquid cultures at LL and after switch to HL for 24 h. The S1 ribosomal protein was used as a loading control. Relative change between the two light conditions is quantified in the plot on the right, showing mean and standard deviation (error bars) from three independent experiments. Additional data can be found in Figures S6C–S6F.

(C–K) *In situ* cryo-ET of WT (C–E), F4E (F–H), and V11E (I–K) cells in liquid culture after switching to HL for 24 h. Left panels: multiple cells in low-magnification transmission EM overviews after cryo-FIB milling. Center panels: 2D slices through tomographic volumes (see additional examples in Figure S6G). Right panels: 3D segmentations of the tomograms (dark green, thylakoid membranes; light green, thylakoid lumen; three shades of blue, outer membrane, peptidoglycan layer, and plasma membrane; brown/pink, carboxysomes; gray, lipid droplet; yellow, defective convergence membrane). A red arrowhead indicates abnormal convergence zone architecture (see more examples in Figure S7).

(L) For each strain and condition, quantification of median thylakoid lumen width (red line) along with 25%–75% percentiles (box) and 1.5× interquartile range (whiskers). n = 283 thylakoid membrane regions from 48 tomograms.

(M–O) Tomographic overview (M), close-up (N), and 3D segmentation (O) of an *in situ* structure that resembles a protein coat (yellow) encapsulating a membrane (blue) in close contact with a thylakoid (green).

Scale bars: 2 μm (C, F, and I), 200 nm (D, G, J, and M), and 40 nm (N). See also Video S3.

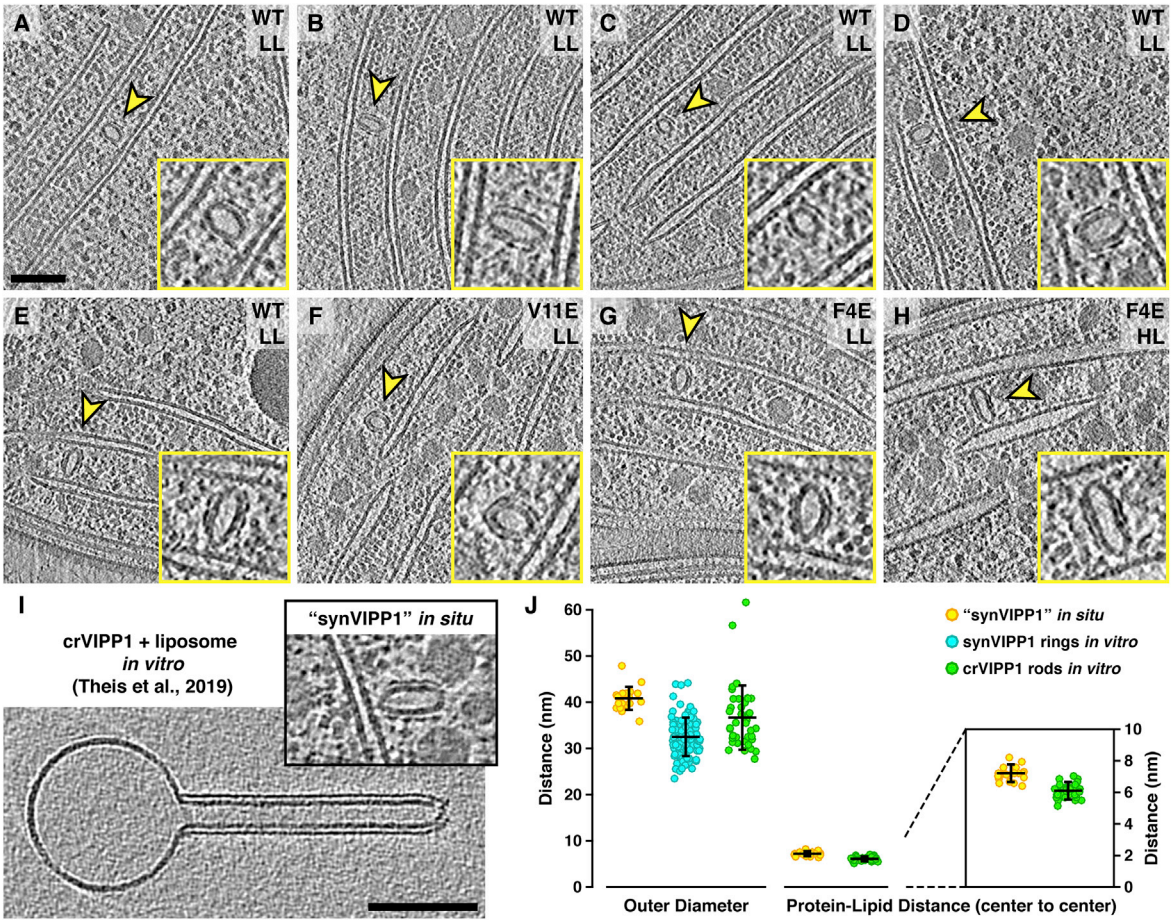

Figure 5. Putative *syn*VIPP1 structures visualized inside native *Synechocystis* cells by *in situ* cryo-ET

(A–H) 2D slices through tomographic volumes showing membranes encapsulated in a protein coat (indicated by yellow arrowheads in the overviews and enlarged 2× in the yellow inset panels). These putative *syn*VIPP1-coated membranes were always observed closely associated with a thylakoid membrane, roughly perpendicular to the thylakoid surface. Strain and growth condition are indicated.

(I) Comparison of one of the *in situ* putative *syn*VIPP1 structures (labeled "synVIPP1") with an *in vitro cr*VIPP1 rod encapsulating a liposome (the liposome on the left is engulfed by VIPP1 on the right; modified from Theis et al., 2019). Both images are shown at the same scale.

(J) Measurement of the outer diameter across the short central axis of *in situ* putative *syn*VIPP1 structures (yellow), *in vitro syn*VIPP1 rings (blue, from raw micrographs such as in Figure S1B), and *in vitro cr*VIPP1 rods (green; Theis et al., 2019). For *in situ* putative *syn*VIPP1 and *in vitro cr*VIPP1, the distance is also measured from the center of the protein coat density to the center of the enclosed lipid bilayer density (enlarged in the inset). The cellular membranes were thicker than the liposomes, resulting in a slightly larger *in situ* distance. Horizontal black lines, mean values; error bars, standard deviations.

Scale bars: 100 nm. See also *in situ syn*VIPP1-GFP in Figure S8.

concurrent studies on VIPP1 and PspA structure (Junglas et al., 2021; Liu et al., 2021 [this issue of *Cell*]), which adapt the numbering of VIPP1/PspA α helices to the ESCRT-III nomenclature (H1 becomes α0, H2 becomes α1, etc.). Liu et al. (2021) further performed bioinformatics analyses based on sequence conservation and found that VIPP1, PspA, and ESCRT-III belong to one superfamily with a shared evolutionary origin. Like VIPP1 and PspA, ESCRT-III plays important roles in repairing cellular membranes (Hurley, 2015). In mammalian cells, ESCRT-III has been implicated in nuclear envelope repair (Denais et al., 2016; Raab et al., 2016) and mitotic reformation (Olmos et al., 2015; Vietri et al., 2015) as well as repair of the plasma membrane (Jimenez et al., 2014; Scheffer et al., 2014). One notable difference between VIPP1 and ESCRT-III is that VIPP1 rings directly bind and hydrolyze nucleotides (Figure 2), whereas ESCRT-III assemblies interact with the AAA-ATPase Vps4 to mediate subunit exchange and helical filament constriction, thereby driving membrane remodeling (Mierzwa et al., 2017; Schöneberg et al., 2018; Maity et al., 2019; Pfitzner et al., 2020).

VIPP1 forms stacked rings and helical rods of variable pitch and handedness

VIPP1 can assemble into a wide variety of oligomeric architectures. *In vitro*, *syn*VIPP1 primarily forms rings, whereas *cr*VIPP1 more frequently makes extended rods (Liu et al., 2007; Fuhrmann et al., 2009a; Saur et al., 2017; Theis et al., 2019). Rings and rods are closely related conformations that oligomerize via very similar

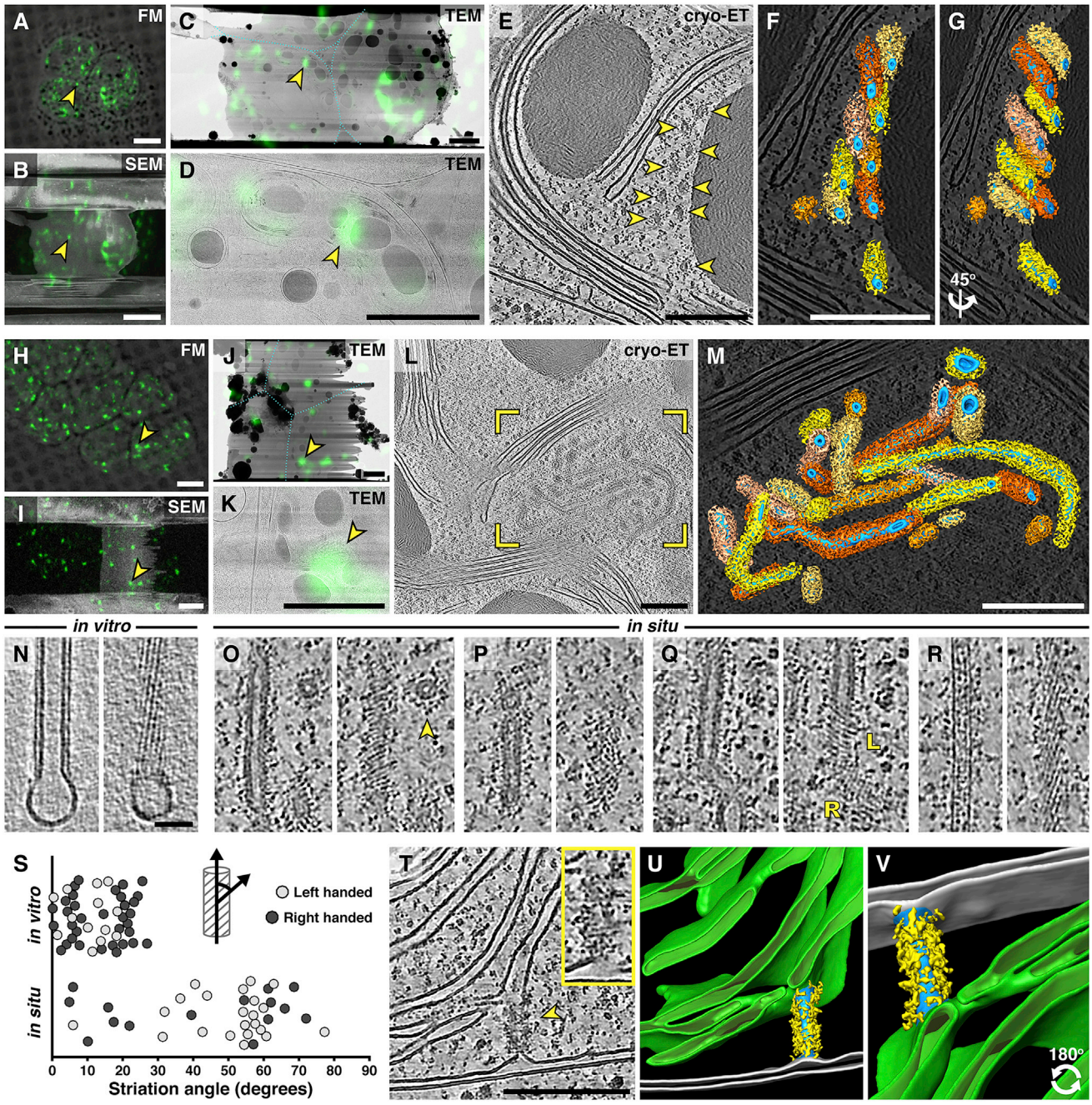

Figure 6. Cryo-correlative light and EM (cryo-CLEM) of *cr*VIPP1-mCherry in *Chlamydomonas* cells

(A–M) Two cryo-CLEM workflows on different cells, with mCherry fluorescence shown in green. Correlated positions of fluorescent puncta between images are marked with yellow arrowheads. Workflow steps are displayed with (A and H) cryo-fluorescence microscopy (FM), (B and I) scanning EM (SEM) after cryo-FIB milling, (C and J) transmission EM (TEM) overviews of the milled lamellae, and (D and K) enlarged TEM close-ups. Cell boundaries are traced in the overviews with dotted blue lines. The large dark cellular structures are starch granules and acidocalcisomes. In the localized regions, we show (E and L) 2D slices through cryo-ET volumes and (F, G, and M) 3D segmentations of the VIPP1-coated membrane tubules indicated by arrowheads in (E) and the boxed region in (L). Encapsulated membrane tubules are displayed in blue, and *cr*VIPP1-mCherry coats range from yellow to dark orange. The view in (G) is tilted 45° from that in (F).

(N) A *cr*VIPP1 rod (not decorated with mCherry) assembled *in vitro*, which subsequently encapsulated a liposome (from Theis et al., 2019).

(O–R) Four examples of *cr*VIPP1-mCherry membrane tubule structures *in situ*, displayed at the same scale (arrowhead, tubule in cross-section). Although many *cr*VIPP1 coats showed ordered helical striations (O), other coats appeared less ordered (P).The *cr*VIPP1 coat in (Q) changes handedness (R, right-handed; L, left-handed), as observed previously *in vitro* (Theis et al., 2019). The *cr*VIPP1 helical rod in (R) lacks the same type of encapsulated membrane bilayers as seen in (O)–(Q).

(legend continued on next page)

interactions (Junglas et al., 2021). Rings and rods adopt various symmetries, with corresponding changes in diameter (Figures 1H and S1K), and rods also vary in their helical pitch and even their handedness (Theis et al., 2019). We observed that single mutations in the H1 helix shift the equilibrium of *syn*VIPP1 oligomerization from rings to rods (Figures 3D–3F and S5), indicating that VIPP1 is on a tipping point between these two architectures. Because H1 binds lipids in the VIPP1 ring lumen (Figures 3A–3C), it is possible that membrane interactions may influence the ring-rod decision. Previous work has shown that H1 is unstructured in solution and acquires an α-helical structure upon interaction with lipids (McDonald et al., 2017). Given the stabilizing interactions between H1 columns and the ring wall (Figures 1C and S2C), it is conceivable that lipid binding converts H1 into an α helix, which then enables H1 to form columns along the VIPP1 wall, shifting the *in vitro* equilibrium from parallel rod to tapered ring architecture. However, pre-formed *cr*VIPP1 rods can subsequently encapsulate liposomes *in vitro* without triggering a dramatic conversion to ring structures (Theis et al., 2019). Such a situation was recently examined for PspA rods (Junglas et al., 2021), where the H1 helix was only seen upon membrane encapsulation, supporting the idea that lipid interactions structure H1.

In situ, *cr*VIPP1 assembles into membrane-encapsulating rod-like structures with right- and left-handed helices that also adopt a wide range of diameters and pitches (Figure 6). Although we initially found VIPP1's oligomeric heterogeneity surprising, it has been demonstrated that single mutations can cause extensive changes to the quaternary structure of coiled-coil helical assemblies (Egelman et al., 2015). Indeed, this heterogeneity may enable VIPP1 coats to accommodate a wide range of membrane curvatures during the biogenesis and maintenance of thylakoids.

Nucleotide hydrolysis and the polarity of VIPP1 oligomerization

Like actin filaments and microtubules, VIPP1 rings (and, presumably, also rods) are polar structures that bind and hydrolyze nucleotides. However, unlike these cytoskeletal structures, VIPP1 rings do not retain nucleotides bound along their lengths. It remains to be described whether and how nucleotide binding and hydrolysis are coordinated with VIPP1 oligomerization. The VIPP1 structures in our study hint at two distinct possible mechanisms depending on the polarity of oligomer assembly (Figure 7). If layer 1 is the first to assemble, then nucleotide binding and hydrolysis may only promote initial nucleation of the ring structure, and subsequent extension of the structure would proceed without nucleotide binding. If layer 1 is the last to assemble, then it is possible that oligomerization proceeds through a cycle of nucleotide binding, hydrolysis, and release as layers are added sequentially. If VIPP1 oligomerization is nucleated on membranes, then this "hydrolysis and release" mechanism could potentially produce the thylakoid-associated putative VIPP1 structures we observed in *Synechocystis* cells (Figures 4M–4O and 5) as well as the VIPP1-coated membrane tubules we observed in *Chlamydomonas* cells (Figure 6). VIPP1's amphipathic H1 helix has a high affinity for anionic lipids (Otters et al., 2013; Hennig et al., 2015; Theis et al., 2019) and can sense stored curvature elastic (SCE) stress (McDonald et al., 2015; McDonald et al., 2017). These two affinities may be related because anionic lipids favor curved membranes due to repulsion between their head groups (Hirama et al., 2017). Thus, we speculate that VIPP1 may concentrate in regions with increased SCE and/or anionic lipids and oligomerize into ring and rod structures that suck up lipids as they extend from the membrane (Figure 7).

VIPP1's nucleotide binding pocket is likely conserved with PspA, which has also been observed to hydrolyze GTP (Ohnishi et al., 2018). When assembled, VIPP1 rings and rods are rather stable but can be disassembled efficiently by HSP70B-CDJ2-CGE1 chaperones (Liu et al., 2005, 2007). The interplay of membrane interaction, nucleotide hydrolysis, and chaperone binding may regulate the *in vivo* dynamics of VIPP1 oligomerization.

The role of VIPP1 in thylakoid biogenesis

The molecular structures described in our study provide a starting point for unraveling the essential *in vivo* function of VIPP1 in thylakoid biogenesis. In algae and plants, thylakoid lipids originate in the chloroplast envelope (Kobayashi, 2016). However, the two membrane systems are separate, raising the question of how lipids are delivered from the envelope to the thylakoids. Because VIPP1 binds lipids and is required for thylakoid biogenesis (Kroll et al., 2001; Westphal et al., 2001; Fuhrmann et al., 2009b; Zhang et al., 2012), it has been proposed to be involved in lipid transport. Our observation of a VIPP1-coated membrane tubule connecting thylakoids with the chloroplast envelope in *Chlamydomonas* (Figures 6T–6V) provides a tantalizing hint that VIPP1 may indeed mediate lipid exchange between these compartments. Consistent with this idea, rare connections between thylakoids and the chloroplast envelope were previously reported in *Chlamydomonas* cells expressing WT levels of VIPP1 protein (Engel et al., 2015).

Synechocystis thylakoid convergence zones, where thylakoids merge into high-curvature membranes that make close contact with the plasma membrane, have been implicated in the biogenesis of thylakoids and photosystem II (Stengel et al., 2012; Rast et al., 2015; Heinz et al., 2016; Rast et al., 2019). In low and high light, the F4E and V11E mutants had aberrant convergence zones that lacked thylakoid connectivity and contact sites with the plasma membrane. Instead, these regions frequently contained clusters of round membranes that were filled with a variety of cytosolic material, including ribosomes, glycogen granules, and phycobilisomes (Figures S7). Similar aberrant structures at thylakoid convergence zones have been observed in *Chlamydomonas* upon VIPP1 knockdown (Nordhues et al., 2012). Thus, the

(S) Quantification of the striation angle (angle between the rod long axis and inclination of the VIPP1 striations) and handedness in the *in vitro* and *in situ* datasets. (T–V) A *cr*VIPP1 coat mediating a membrane continuity between thylakoids and the chloroplast envelope. Shown are (T) 2D slices through the tomogram (the VIPP1 structure marked with the arrowhead is enlarged in the inset) and (U and V) corresponding 3D segmentations (green, thylakoids; gray, chloroplast envelope; yellow, *cr*VIPP1-mCherry; blue, membrane encapsulated in the VIPP1 coat). The view in (V) is rotated 180° from that in (U). *In situ* VIPP1-mCherry structures were observed in a total of 23 tomograms.

Scale bars: 5 μm (A, B, H, and I), 2 μm (C, D, J, and K), 200 nm (E, F, L, M, and T), and 40 nm (N-R and inset in T). See also Videos S4, S5, and S6.

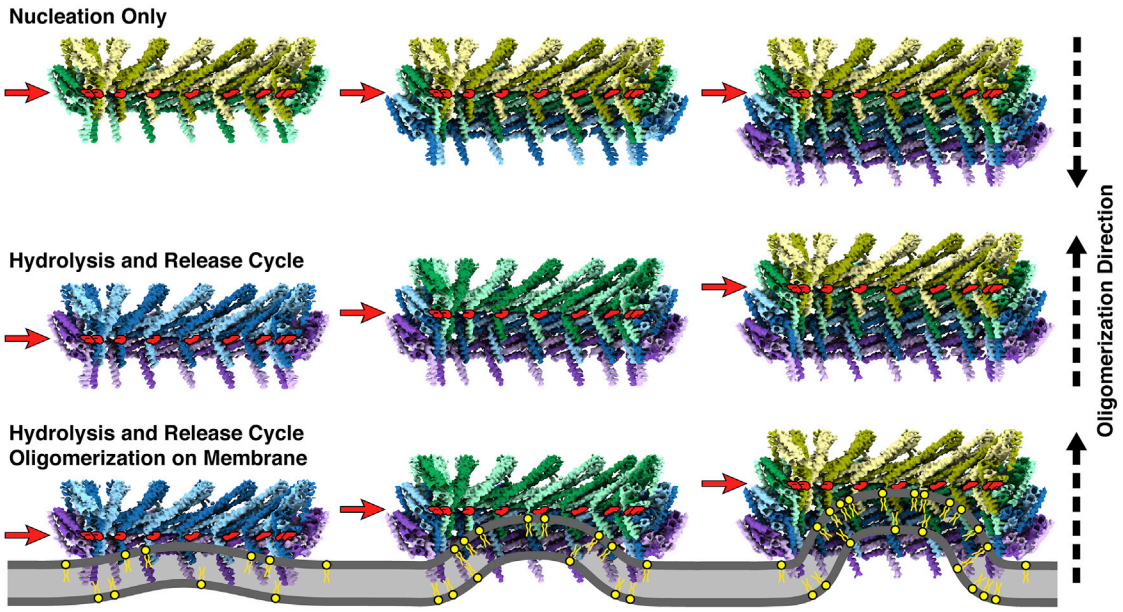

Figure 7. Hypothetical models for the polarized assembly of VIPP1 rings

In the "nucleation only" model (top row), ring structures are nucleated by binding and hydrolysis of nucleotides between layers 1 and 2, the same position where ADP densities are observed in the final cryo-EM density maps (nucleotide positions are marked with red arrows). Oligomerization then proceeds sequentially to layers 3, 4, and so on without additional nucleotide binding. In the "hydrolysis and release" model (center row), ring structures are nucleated on the opposite end from layer 1 (the nucleotide is shown between layers 3 and 4 here, but it would start between layers 5 and 6 in the C16 ring from Figure 1). After hydrolysis, the nucleotide is released, and then more nucleotide is bound and hydrolyzed as a new layer is added (center panel). This cycle continues until layers cannot be added, presumably because of the inclination of layer 1 (Figures S1I and S1J). Regardless of the direction of oligomerization (indicated by dashed arrows on the right of the figure), the final structure looks the same in both models, with nucleotide bound between layers 1 and 2. The "hydrolysis and release" model is more consistent with oligomerization of VIPP1 on a membrane (bottom row). In such a mechanism, VIPP1 monomers interact with the thylakoid membrane (gray) through their amphipathic H1 helix and begin to concentrate at regions with abundant SCE stress and/or anionic lipids (yellow). VIPP1 monomers oligomerize into a membrane-anchored ring structure that extends by "hydrolysis and release," adding new layers farther and farther from the membrane. As the VIPP1 ring extends, lipids are sucked from the thylakoid into the growing ring lumen. The increased membrane curvature and affinity for H1 could potentially concentrate anionic lipids in this encapsulated membrane.

interaction of VIPP1 with membranes is likely important for shaping WT convergence zone architecture in cyanobacteria and green algae. Interestingly, despite their defective convergence zones, the F4E and V11E mutants were able to assemble multi-layered thylakoid networks that contained relatively WT levels of photosynthetic proteins (Figures S6C and S6D).

The role of VIPP1 in protecting thylakoids from environmental stress

Our study poses the major questions of how high light causes thylakoid swelling and how VIPP1 counteracts this force to maintain thylakoid architecture. Consistent with our observations in *Synechocystis* (Figure 4L), light-induced swelling of the thylakoid lumen was previously reported in *Arabidopsis* (Kirchhoff et al., 2011). The authors propose that swelling is caused by changes in luminal pH and a resulting increase in osmotic pressure, perhaps mediated by thylakoid-embedded ion channels. In addition to lumen acidification, high light also leads to the generation of reactive oxygen species (Barber, 1995; Pospíšil, 2016), which might exacerbate thylakoid swelling by destabilizing thylakoid proteins and lipids.

At this point, we can only speculate about how VIPP1 counteracts thylakoid swelling, but several recent studies and our own observations provide some hints. Swollen thylakoids have been reported in *Chlamydomonas* and *Arabidopsis* VIPP1 knockdown cells exposed to high light intensities (Nordhues et al., 2012; Zhang et al., 2012). Here we observed thylakoid swelling in the *Synechocystis* F4E and V11E mutants under high light (Figures 4F–4L and S6G), confirming the conservation of this phenotype between cyanobacteria and chloroplasts and specifically implicating lipid-binding hydrophobic residues in VIPP1's H1 helix. PspA can bind damaged bacterial membranes and prevent H^+ leakage *in vitro* (Kobayashi et al., 2007) and *in vivo* (Kleerebezem et al., 1996). Perhaps VIPP1 serves a similar function for thylakoids. VIPP1 membrane binding was recently observed to be enhanced by acidic conditions *in vitro* (Siebenaller et al., 2020), implying that VIPP1 may be able to sense H^+ leakage in stressed thylakoid regions. Two other recent *in vitro* studies observed that *syn*VIPP1 rings and PspA rods can disassemble upon contact with liposomes and coat broad regions of the membrane (Junglas et al., 2020a, 2021). Furthermore, coating liposomes with VIPP1 has been shown to stabilize these membranes against H^+ leakage (Junglas et al., 2020a). It remains to be seen whether such large VIPP1-coated regions can form on native thylakoid sheets, which are composed of ~70% protein (Szalontai et al., 2000). However, it is possible that small VIPP1

patches or even VIPP1 monomers in the membrane could be stabilizing. Consistent with this hypothesis, we observed a ~3-fold reduction in thylakoid-bound putative *syn*VIPP1 structures under high-light conditions (Figure S8G). Perhaps the putative *syn*VIPP1 structures disassemble into the membrane under high-light stress to enhance thylakoid stability and then reform out of the membrane (as diagrammed in Figure 7) upon return to low-light conditions. We emphasize that such a model remains highly speculative and requires further experimental investigation. There may also be non-acute elements of VIPP1's protective function; for example, we observed defective convergence zones and moderate thylakoid swelling in the F4E and V11E mutants even under constant low light (Figure 4).

Limitations of the study

Our study raises many questions that require further investigation. Although nucleotide densities were clearly resolved bound to our VIPP1 ring structures (Figure S3A), and the binding pocket model is supported by functional mutagenesis assays (Figure 2H), our cryo-EM maps have insufficient resolution to directly observe how nucleotide binding and hydrolysis are coordinated. Pushing the resolution further would reveal these details, but it is a challenging task because of the asymmetric occupancy of nucleotides on one end of the VIPP1 ring. In the absence of improved resolution, molecular dynamics simulations may provide insights. One of the biggest mysteries raised by our study is the link between nucleotide hydrolysis and VIPP1 function. Although we find evidence of hydrolysis-dependent VIPP1 oligomerization *in vitro* (Figures 2H and 3F), it was previously shown that *syn*VIPP1 protein denatured in urea can reassemble in buffer lacking nucleotide to form ring-like structures, arguing against the requirement of nucleotide for *in vitro* oligomerization (Aseeva et al., 2004). The models presented in Figure 7 are quite speculative and require detailed investigation, ideally with a reconstituted system that can precisely follow the dynamics of VIPP1 assembly from monomers into rings and rods. The *in vivo* relevance of nucleotide hydrolysis remains unknown and would benefit from mutagenesis experiments—what is the phenotype of the hydrolysis-dead E126Q+E179Q double mutant in *Synechocystis*, and how does mutating these residues affect formation of *in situ* rod-like structures in *Chlamydomonas*? An additional layer of complexity is the flexible H7 domain, which decorates the outside surfaces of VIPP1 rings and rods but is not resolved in our structures (Figure 1). How do interactions with this domain regulate VIPP1 dynamics and impart its thylakoid-specific functions?

Another major question is how the VIPP1 ring and rod structures detailed in our study relate to VIPP1's essential functions in thylakoid biogenesis and maintenance. Our results emphasize the physiological importance of lipid binding by the luminal H1 domain (Figure 4). VIPP1 oligomers likely play a role *in vivo*, as we observed rod-like VIPP1 structures tubulating membranes within the cell and even mediating contact between thylakoids and the chloroplast envelope (Figure 6). However, membrane maintenance functions have also been proposed for "carpets" of VIPP1 monomers (Junglas et al., 2020a, 2021). Based on the disorganized coats we often observed *in situ* (Figures 6P and 6T), we believe that VIPP1 is likely more dynamic inside the cell than what we observed in our *in vitro* structures. It will be illuminating to determine whether additional factors sequentially regulate VIPP1 oligomer architecture to direct membrane-remodeling functions, as shown for ESCRT-III (Pfitzner et al., 2020). We also must emphasize that these *in situ* VIPP1-tubulated membranes were formed in *Chlamydomonas* cells overexpressing VIPP1-mCherry, and, thus, they likely do not occur with such abundance in WT cells. However, overexpression has been used previously to accurately visualize the *in situ* architecture of mammalian ESCRT-III and bacterial ParM assemblies (Salje et al., 2009; McCullough et al., 2015).

It is now clear that membrane remodeling by the ESCRT-III superfamily is widespread throughout bacteria, archaea, fungi, plants, and animals. Within this superfamily, VIPP1 is highly conserved in thylakoid-bearing photosynthetic organisms, from land crops that feed billions of people to marine algae and cyanobacteria that fix half of the Earth's CO_2. Although much remains to be discovered, our study lays the structural foundation for a mechanistic understanding of VIPP1-mediated thylakoid biogenesis and stress resistance across the photosynthetic tree of life.

STAR★METHODS

Detailed methods are provided in the online version of this paper and include the following:

- KEY RESOURCES TABLE
- RESOURCE AVAILABILITY
  - Lead contact
  - Materials availability
  - Data and code availability
- EXPERIMENTAL MODEL AND SUBJECT DETAILS
  - *Synechocystis* sp. PCC 6803
  - *Chlamydomonas reinhardtii*
  - Generation of *Synechocystis* mutant strains
  - Cloning of the VIPP1-mCherry construct and transformation into *Chlamydomonas*
- METHOD DETAILS
  - *syn*VIPP1 and *cr*VIPP1 vector design, protein expression and purification
  - Negative-stain EM data acquisition
  - Cryo-EM data acquisition
  - Cryo-EM image processing and single particle analysis
  - Modeling of VIPP1 into the cryo-EM density
  - Detection of VIPP1-bound nucleotide by mass spectrometry
  - VIPP1 nucleotide hydrolysis assays
  - Physiological and biochemical analysis of *Synechocystis* mutants
  - *Synechocystis* vitrification, cryo-FIB milling, and cryo-ET data acquisition
  - *Chlamydomonas* vitrification and cryo-CLEM workflow
  - *In situ* cryo-ET reconstruction, denoising, and segmentation
- QUANTIFICATION AND STATISTICAL ANALYSIS
  - Estimation of the distribution of rings and rods in *syn*VIPP1 mutant proteins
  - *In situ* cryo-ET measurements

SUPPLEMENTAL INFORMATION

Supplemental information can be found online at https://doi.org/10.1016/j.cell.2021.05.011.

ACKNOWLEDGMENTS

We thank Conrad Mullineaux for generously providing the *Synechocystis vipp1-GFP* strain; Elisabeth Weyher-Stingl and Victoria Sanchez Caballero at the MPI Biochemistry core facility for assistance with mass spectrometry; Ricardo Righetto for performing data deposition; Günter Pfeifer and Florian Beck for help with microscopy and image analysis; Alexander Hertle, Ralph Bock, Christin Radon, and Petra Wendler for assistance with CLEM experiments; Gert Bange for helpful discussions; and Karin Engel for critically reading the manuscript. J.M.P. thanks Leica for a collaboration to develop the prototype cryo-confocal microscope. This work was supported by grants from the Deutsche Forschungsgemeinschaft to J.N. (NI 390/9-2 as part of FOR2092), J.M.S. (Emmy Noether grant SCHU 3364/1-1), M.S. (Schr 617/8-2 as part of FOR2092 and TRR 175 project C02), and B.D.E. (EN 1194/1-1 as part of FOR2092), as well as KAKENHI grants to W.S. (16H06554 from the Ministry of Education, Culture, Sports, Science and Technology and 21H02508 from the Japanese Society for the Promotion of Science). Additional funding was provided by the Max Planck Society, the Helmholtz Zentrum München, and LMU Munich's Institutional Strategy "LMU Excellent" within the framework of the German Excellence Initiative.

AUTHOR CONTRIBUTIONS

Cryo-EM data acquisition and structure determination were performed by T.K.G. with guidance from J.M.S. Molecular modeling was performed by S.K. with guidance from T.R. Cloning and production of VIPP1 proteins was performed by K.G. and J. Niemeyer with guidance from M. Schroda. Creation and physiological characterization of the *Synechocystis* VIPP1 mutants was performed by S.H. with guidance from J. Nickelsen. *In situ* cryo-ET data acquisition and analysis were performed by W.W. and S.K. with help from M. Schaffer, A.R., and B.D.E. Additional protein purification and nucleotide hydrolysis assays were performed by N.O. with guidance from W.S. The *Chlamydomonas* VIPP1-mCherry strain was made by B.S. with guidance from M. Schroda. The cryo-CLEM studies were performed by W.W. and S.K. with assistance from M.O. M. Strauss aided with preliminary negative-stain EM image analysis of *syn*VIPP1 rings. W.B. and J.M.P. provided guidance, financial support, and access to instrumentation. T.K.G., J.M.S., M. Schroda, and B.D.E. wrote the paper with input from all authors.

DECLARATION OF INTERESTS

The authors declare no competing interests.

Received: August 3, 2020
Revised: February 16, 2021
Accepted: May 10, 2021
Published: June 23, 2021

REFERENCES

Arnold, J., Mahamid, J., Lucic, V., de Marco, A., Fernandez, J.J., Laugks, T., Mayer, T., Hyman, A.A., Baumeister, W., and Plitzko, J.M. (2016). Site-Specific Cryo-focused Ion Beam Sample Preparation Guided by 3D Correlative Microscopy. Biophys. J. *110*, 860–869.

Asano, S., Engel, B.D., and Baumeister, W. (2016). In Situ Cryo-Electron Tomography: A Post-Reductionist Approach to Structural Biology. J. Mol. Biol. *428* (2 Pt A), 332–343.

Aseeva, E., Ossenbühl, F., Eichacker, L.A., Wanner, G., Soll, J., and Vothknecht, U.C. (2004). Complex formation of Vipp1 depends on its α-helical PspA-like domain. J. Biol. Chem. *279*, 35535–35541.

Aseeva, E., Ossenbühl, F., Sippel, C., Cho, W.K., Stein, B., Eichacker, L.A., Meurer, J., Wanner, G., Westhoff, P., Soll, J., and Vothknecht, U.C. (2007). Vipp1 is required for basic thylakoid membrane formation but not for the assembly of thylakoid protein complexes. Plant Physiol. Biochem. *45*, 119–128.

Banerjee, S., Bartesaghi, A., Merk, A., Rao, P., Bulfer, S.L., Yan, Y., Green, N., Mroczkowski, B., Neitz, R.J., Wipf, P., et al. (2016). 2.3 Å resolution cryo-EM structure of human p97 and mechanism of allosteric inhibition. Science *351*, 871–875.

Barber, J. (1995). Molecular Basis of the Vulnerability of Photosystem II to Damage by Light. Funct. Plant Biol. *22*, 201–208.

Bäuerlein, F.J.B., Saha, I., Mishra, A., Kalemanov, M., Martínez-Sánchez, A., Klein, R., Dudanova, I., Hipp, M.S., Hartl, F.U., Baumeister, W., and Fernández-Busnadiego, R. (2017). In Situ Architecture and Cellular Interactions of PolyQ Inclusions. Cell *171*, 179–187.e10.

Bryan, S.J., Burroughs, N.J., Shevela, D., Yu, J., Rupprecht, E., Liu, L.-N., Mastroianni, G., Xue, Q., Llorente-Garcia, I., Leake, M.C., et al. (2014). Localisation and interactions of the Vipp1 protein in cyanobacteria. Mol. Microbiol. *94*, 1179–1195.

Buchholz, T.-O., Jordan, M., Pigino, G., and Jug, F. (2018). Cryo-CARE: Content-Aware Image Restoration for Cryo-Transmission Electron Microscopy Data. arXiv, arXiv:1810.05420. https://arxiv.org/abs/1810.05420.

Cardone, G., Heymann, J.B., and Steven, A.C. (2013). One number does not fit all: mapping local variations in resolution in cryo-EM reconstructions. J. Struct. Biol. *184*, 226–236.

Chauhan, J.S., Mishra, N.K., and Raghava, G.P. (2009). Identification of ATP binding residues of a protein from its primary sequence. BMC Bioinformatics *10*, 434.

Chauhan, J.S., Mishra, N.K., and Raghava, G.P.S. (2010). Prediction of GTP interacting residues, dipeptides and tripeptides in a protein from its evolutionary information. BMC Bioinformatics *11*, 301.

Crozet, P., Navarro, F.J., Willmund, F., Mehrshahi, P., Bakowski, K., Lauersen, K.J., Pérez-Pérez, M.E., Auroy, P., Gorchs Rovira, A., Sauret-Gueto, S., et al. (2018). Birth of a Photosynthetic Chassis: A MoClo Toolkit Enabling Synthetic Biology in the Microalga Chlamydomonas reinhardtii. ACS Synth. Biol. *7*, 2074–2086.

Darwin, A.J. (2013). Stress relief during host infection: The phage shock protein response supports bacterial virulence in various ways. PLoS Pathog. *9*, e1003388.

DeLisa, M.P., Lee, P., Palmer, T., and Georgiou, G. (2004). Phage shock protein PspA of Escherichia coli relieves saturation of protein export via the Tat pathway. J. Bacteriol. *186*, 366–373.

Denais, C.M., Gilbert, R.M., Isermann, P., McGregor, A.L., te Lindert, M., Weigelin, B., Davidson, P.M., Friedl, P., Wolf, K., and Lammerding, J. (2016). Nuclear envelope rupture and repair during cancer cell migration. Science *352*, 353–358.

Eaton-Rye, J.J. (2004). The construction of gene knockouts in the cyanobacterium Synechocystis sp. PCC 6803. Methods Mol. Biol. *274*, 309–324.

Egelman, E.H., Xu, C., DiMaio, F., Magnotti, E., Modlin, C., Yu, X., Wright, E., Baker, D., and Conticello, V.P. (2015). Structural plasticity of helical nanotubes based on coiled-coil assemblies. Structure *23*, 280–289.

Engel, B.D., Schaffer, M., Kuhn Cuellar, L., Villa, E., Plitzko, J.M., and Baumeister, W. (2015). Native architecture of the Chlamydomonas chloroplast revealed by in situ cryo-electron tomography. eLife *4*, e04889.

Fuhrmann, E., Bultema, J.B., Kahmann, U., Rupprecht, E., Boekema, E.J., and Schneider, D. (2009a). The vesicle-inducing protein 1 from Synechocystis sp. PCC 6803 organizes into diverse higher-ordered ring structures. Mol. Biol. Cell *20*, 4620–4628.

Fuhrmann, E., Gathmann, S., Rupprecht, E., Golecki, J., and Schneider, D. (2009b). Thylakoid membrane reduction affects the photosystem stoichiometry in the cyanobacterium Synechocystis sp. PCC 6803. Plant Physiol. *149*, 735–744.

Gat, Y., Schuller, J.M., Lingaraju, M., Weyher, E., Bonneau, F., Strauss, M., Murray, P.J., and Conti, E. (2019). InsP_6 binding to PIKK kinases revealed by

the cryo-EM structure of an SMG1-SMG8-SMG9 complex. Nat. Struct. Mol. Biol. *26*, 1089–1093.

Goddard, T.D., Huang, C.C., Meng, E.C., Pettersen, E.F., Couch, G.S., Morris, J.H., and Ferrin, T.E. (2018). UCSF ChimeraX: Meeting modern challenges in visualization and analysis. Protein Sci. *27*, 14–25.

Goh, B.C., Hadden, J.A., Bernardi, R.C., Singharoy, A., McGreevy, R., Rudack, T., Cassidy, C.K., and Schulten, K. (2016). Computational Methodologies for Real-Space Structural Refinement of Large Macromolecular Complexes. Annu. Rev. Biophys. *45*, 253–278.

Gutu, A., Chang, F., and O'Shea, E.K. (2018). Dynamical localization of a thylakoid membrane binding protein is required for acquisition of photosynthetic competency. Mol. Microbiol. *108*, 16–31.

Hagen, W.J.H., Wan, W., and Briggs, J.A.G. (2017). Implementation of a cryo-electron tomography tilt-scheme optimized for high resolution subtomogram averaging. J. Struct. Biol. *197*, 191–198.

Hamelryck, T., and Manderick, B. (2003). PDB file parser and structure class implemented in Python. Bioinformatics *19*, 2308–2310.

Hankamer, B.D., Elderkin, S.L., Buck, M., and Nield, J. (2004). Organization of the AAA(+) adaptor protein PspA is an oligomeric ring. J. Biol. Chem. *279*, 8862–8866.

He, S., Chou, H.-T., Matthies, D., Wunder, T., Meyer, M.T., Atkinson, N., Martinez-Sanchez, A., Jeffrey, P.D., Port, S.A., Patena, W., et al. (2020). The structural basis of Rubisco phase separation in the pyrenoid. Nat. Plants *6*, 1480–1490.

Heinz, S., Rast, A., Shao, L., Gutu, A., Gügel, I.L., Heyno, E., Labs, M., Rengstl, B., Viola, S., Nowaczyk, M.M., et al. (2016). Thylakoid Membrane Architecture in *Synechocystis* Depends on CurT, a Homolog of the Granal CURVATURE THYLAKOID1 Proteins. Plant Cell *28*, 2238–2260.

Hennig, R., Heidrich, J., Saur, M., Schmüser, L., Roeters, S.J., Hellmann, N., Woutersen, S., Bonn, M., Weidner, T., Markl, J., and Schneider, D. (2015). IM30 triggers membrane fusion in cyanobacteria and chloroplasts. Nat. Commun. *6*, 7018.

Hennig, R., West, A., Debus, M., Saur, M., Markl, J., Sachs, J.N., and Schneider, D. (2017). The IM30/Vipp1 C-terminus associates with the lipid bilayer and modulates membrane fusion. Biochim. Biophys. Acta Bioenerg. *1858*, 126–136.

Hirama, T., Lu, S.M., Kay, J.G., Maekawa, M., Kozlov, M.M., Grinstein, S., and Fairn, G.D. (2017). Membrane curvature induced by proximity of anionic phospholipids can initiate endocytosis. Nat. Commun. *8*, 1393.

Humphrey, W., Dalke, A., and Schulten, K. (1996). VMD: visual molecular dynamics. J. Mol. Graph. *14*, 33–38, 27–38.

Hurley, J.H. (2015). ESCRTs are everywhere. EMBO J. *34*, 2398–2407.

Jimenez, A.J., Maiuri, P., Lafaurie-Janvore, J., Divoux, S., Piel, M., and Perez, F. (2014). ESCRT machinery is required for plasma membrane repair. Science *343*, 1247136.

Jovanovic, G., Mehta, P., McDonald, C., Davidson, A.C., Uzdavinys, P., Ying, L., and Buck, M. (2014). The N-terminal amphipathic helices determine regulatory and effector functions of phage shock protein A (PspA) in Escherichia coli. J. Mol. Biol. *426*, 1498–1511.

Junglas, B., Orru, R., Axt, A., Siebenaller, C., Steinchen, W., Heidrich, J., Hellmich, U.A., Hellmann, N., Wolf, E., Weber, S.A.L., and Schneider, D. (2020a). IM30 IDPs form a membrane-protective carpet upon super-complex disassembly. Commun. Biol. *3*, 595.

Junglas, B., Siebenaller, C., Schlösser, L., Hellmann, N., and Schneider, D. (2020b). GTP hydrolysis by Synechocystis IM30 does not decisively affect its membrane remodeling activity. Sci. Rep. *10*, 9793.

Junglas, B., Huber, S.T., Heidler, T., Mann, D., Hennig, R., Clarke, M., Ortiz, J.O., Schneider, D., and Sachse, C. (2021). PspA maintains membrane integrity by an ESCRT-like membrane remodeling activity. Cell *184*. Published online June 23, 2021. https://doi.org/10.1016/j.cell.2021.05.042.

Kindle, K.L. (1990). High-frequency nuclear transformation of Chlamydomonas reinhardtii. Proc. Natl. Acad. Sci. USA *87*, 1228–1232.

Kirchhoff, H., Hall, C., Wood, M., Herbstová, M., Tsabari, O., Nevo, R., Charuvi, D., Shimoni, E., and Reich, Z. (2011). Dynamic control of protein diffusion within the granal thylakoid lumen. Proc. Natl. Acad. Sci. USA *108*, 20248–20253.

Kleerebezem, M., Crielaard, W., and Tommassen, J. (1996). Involvement of stress protein PspA (phage shock protein A) of Escherichia coli in maintenance of the protonmotive force under stress conditions. EMBO J. *15*, 162–171.

Klein, S., Wimmer, B.H., Winter, S.L., Kolovou, A., Laketa, V., and Chlanda, P. (2021). Post-correlation on-lamella cryo-CLEM reveals the membrane architecture of lamellar bodies. Commun. Biol. *4*, 137.

Kobayashi, K. (2016). Role of membrane glycerolipids in photosynthesis, thylakoid biogenesis and chloroplast development. J. Plant Res. *129*, 565–580.

Kobayashi, R., Suzuki, T., and Yoshida, M. (2007). Escherichia coli phage-shock protein A (PspA) binds to membrane phospholipids and repairs proton leakage of the damaged membranes. Mol. Microbiol. *66*, 100–109.

Kremer, J.R., Mastronarde, D.N., and McIntosh, J.R. (1996). Computer visualization of three-dimensional image data using IMOD. J. Struct. Biol. *116*, 71–76.

Kroll, D., Meierhoff, K., Bechtold, N., Kinoshita, M., Westphal, S., Vothknecht, U.C., Soll, J., and Westhoff, P. (2001). VIPP1, a nuclear gene of Arabidopsis thaliana essential for thylakoid membrane formation. Proc. Natl. Acad. Sci. USA *98*, 4238–4242.

Leaver-Fay, A., Tyka, M., Lewis, S.M., Lange, O.F., Thompson, J., Jacak, R., Kaufman, K.W., Renfrew, P.D., Smith, C.A., Sheffler, W., et al. (2011). Chapter nineteen - Rosetta3: An Object-Oriented Software Suite for the Simulation and Design of Macromolecules. In Methods in Enzymology, M.L. Johnson and L. Brand, eds. (Academic Press), pp. 545–574.

Li, H.M., Kaneko, Y., and Keegstra, K. (1994). Molecular cloning of a chloroplastic protein associated with both the envelope and thylakoid membranes. Plant Mol. Biol. *25*, 619–632.

Liebschner, D., Afonine, P.V., Baker, M.L., Bunkóczi, G., Chen, V.B., Croll, T.I., Hintze, B., Hung, L.W., Jain, S., McCoy, A.J., et al. (2019). Macromolecular structure determination using X-rays, neutrons and electrons: recent developments in Phenix. Acta Crystallogr. D Struct. Biol. *75*, 861–877.

Liu, C., Willmund, F., Whitelegge, J.P., Hawat, S., Knapp, B., Lodha, M., and Schroda, M. (2005). J-domain protein CDJ2 and HSP70B are a plastidic chaperone pair that interacts with vesicle-inducing protein in plastids 1. Mol. Biol. Cell *16*, 1165–1177.

Liu, C., Willmund, F., Golecki, J.R., Cacace, S., Hess, B., Markert, C., and Schroda, M. (2007). The chloroplast HSP70B-CDJ2-CGE1 chaperones catalyse assembly and disassembly of VIPP1 oligomers in Chlamydomonas. Plant J. *50*, 265–277.

Liu, J., Tassinari, M., Souza, D.P., Naskar, S., Noel, J.K., Bohuszewicz, O., Buck, M., Williams, T.A., Baum, B., and Low, H.H. (2021). Bacterial Vipp1 and PspA are members of the ancient ESCRT-III membrane-remodelling superfamily. Cell *184*. Published online June 23, 2021. https://doi.org/10.1016/j.cell.2021.05.011.

Lodha, M., Schulz-Raffelt, M., and Schroda, M. (2008). A new assay for promoter analysis in Chlamydomonas reveals roles for heat shock elements and the TATA box in HSP70A promoter-mediated activation of transgene expression. Eukaryot. Cell *7*, 172–176.

Maity, S., Caillat, C., Miguet, N., Sulbaran, G., Effantin, G., Schoehn, G., Roos, W.H., and Weissenhorn, W. (2019). VPS4 triggers constriction and cleavage of ESCRT-III helical filaments. Sci. Adv. *5*, eaau7198.

Manganelli, R., and Gennaro, M.L. (2017). Protecting from Envelope Stress: Variations on the Phage-Shock-Protein Theme. Trends Microbiol. *25*, 205–216.

Martinez-Sanchez, A., Garcia, I., Asano, S., Lucic, V., and Fernandez, J.J. (2014). Robust membrane detection based on tensor voting for electron tomography. J. Struct. Biol. *186*, 49–61.

Mastronarde, D.N. (2005). Automated electron microscope tomography using robust prediction of specimen movements. J. Struct. Biol. *152*, 36–51.

McCullough, J., Clippinger, A.K., Talledge, N., Skowyra, M.L., Saunders, M.G., Naismith, T.V., Colf, L.A., Afonine, P., Arthur, C., Sundquist, W.I., et al. (2015). Structure and membrane remodeling activity of ESCRT-III helical polymers. Science *350*, 1548–1551.

McDonald, C., Jovanovic, G., Ces, O., and Buck, M. (2015). Membrane Stored Curvature Elastic Stress Modulates Recruitment of Maintenance Proteins PspA and Vipp1. mBio *6*, e01188-–e011815.

McDonald, C., Jovanovic, G., Wallace, B.A., Ces, O., and Buck, M. (2017). Structure and function of PspA and Vipp1 N-terminal peptides: Insights into the membrane stress sensing and mitigation. Biochim. Biophys. Acta Biomembr. *1859*, 28–39.

Michaud-Agrawal, N., Denning, E.J., Woolf, T.B., and Beckstein, O. (2011). MDAnalysis: a toolkit for the analysis of molecular dynamics simulations. J. Comput. Chem. *32*, 2319–2327.

Mierzwa, B.E., Chiaruttini, N., Redondo-Morata, L., von Filseck, J.M., König, J., Larios, J., Poser, I., Müller-Reichert, T., Scheuring, S., Roux, A., and Gerlich, D.W. (2017). Dynamic subunit turnover in ESCRT-III assemblies is regulated by Vps4 to mediate membrane remodelling during cytokinesis. Nat. Cell Biol. *19*, 787–798.

Morris, G.M., Huey, R., Lindstrom, W., Sanner, M.F., Belew, R.K., Goodsell, D.S., and Olson, A.J. (2009). AutoDock4 and AutoDockTools4: Automated docking with selective receptor flexibility. J. Comput. Chem. *30*, 2785–2791.

Neupert, J., Karcher, D., and Bock, R. (2009). Generation of Chlamydomonas strains that efficiently express nuclear transgenes. Plant J. *57*, 1140–1150.

Nguyen, H.C., Talledge, N., McCullough, J., Sharma, A., Moss, F.R., 3rd, Iwasa, J.H., Vershinin, M.D., Sundquist, W.I., and Frost, A. (2020). Membrane constriction and thinning by sequential ESCRT-III polymerization. Nat. Struct. Mol. Biol. *27*, 392–399.

Nordhues, A., Schöttler, M.A., Unger, A.K., Geimer, S., Schönfelder, S., Schmollinger, S., Rütgers, M., Finazzi, G., Soppa, B., Sommer, F., et al. (2012). Evidence for a role of VIPP1 in the structural organization of the photosynthetic apparatus in Chlamydomonas. Plant Cell *24*, 637–659.

Ohnishi, N., Zhang, L., and Sakamoto, W. (2018). VIPP1 Involved in Chloroplast Membrane Integrity Has GTPase Activity in Vitro. Plant Physiol. *177*, 328–338.

Olmos, Y., Hodgson, L., Mantell, J., Verkade, P., and Carlton, J.G. (2015). ESCRT-III controls nuclear envelope reformation. Nature *522*, 236–239.

Osadnik, H., Schöpfel, M., Heidrich, E., Mehner, D., Lilie, H., Parthier, C., Risselada, H.J., Grubmüller, H., Stubbs, M.T., and Brüser, T. (2015). PspF-binding domain PspA1-144 and the PspA·F complex: New insights into the coiled-coil-dependent regulation of AAA+ proteins. Mol. Microbiol. *98*, 743–759.

Otters, S., Braun, P., Hubner, J., Wanner, G., Vothknecht, U.C., and Chigri, F. (2013). The first α-helical domain of the vesicle-inducing protein in plastids 1 promotes oligomerization and lipid binding. Planta *237*, 529–540.

Patron, N.J., Orzaez, D., Marillonnet, S., Warzecha, H., Matthewman, C., Youles, M., Raitskin, O., Leveau, A., Farré, G., Rogers, C., et al. (2015). Standards for plant synthetic biology: a common syntax for exchange of DNA parts. New Phytol. *208*, 13–19.

Pettersen, E.F., Goddard, T.D., Huang, C.C., Couch, G.S., Greenblatt, D.M., Meng, E.C., and Ferrin, T.E. (2004). UCSF Chimera–a visualization system for exploratory research and analysis. J. Comput. Chem. *25*, 1605–1612.

Pfitzner, A.-K., Mercier, V., Jiang, X., Moser von Filseck, J., Baum, B., Šarić, A., and Roux, A. (2020). An ESCRT-III Polymerization Sequence Drives Membrane Deformation and Fission. Cell *182*, 1140–1155.e18.

Phillips, J.C., Braun, R., Wang, W., Gumbart, J., Tajkhorshid, E., Villa, E., Chipot, C., Skeel, R.D., Kalé, L., and Schulten, K. (2005). Scalable molecular dynamics with NAMD. J. Comput. Chem. *26*, 1781–1802.

Pospíšil, P. (2016). Production of Reactive Oxygen Species by Photosystem II as a Response to Light and Temperature Stress. Front. Plant Sci. *7*, 1950.

Punjani, A., Rubinstein, J.L., Fleet, D.J., and Brubaker, M.A. (2017). cryoSPARC: algorithms for rapid unsupervised cryo-EM structure determination. Nat. Methods *14*, 290–296.

Raab, M., Gentili, M., de Belly, H., Thiam, H.R., Vargas, P., Jimenez, A.J., Lautenschlaeger, F., Voituriez, R., Lennon-Duménil, A.M., Manel, N., and Piel, M. (2016). ESCRT III repairs nuclear envelope ruptures during cell migration to limit DNA damage and cell death. Science *352*, 359–362.

Rast, A., Heinz, S., and Nickelsen, J. (2015). Biogenesis of thylakoid membranes. Biochim. Biophys. Acta *1847*, 821–830.

Rast, A., Schaffer, M., Albert, S., Wan, W., Pfeffer, S., Beck, F., Plitzko, J.M., Nickelsen, J., and Engel, B.D. (2019). Biogenic regions of cyanobacterial thylakoids form contact sites with the plasma membrane. Nat. Plants *5*, 436–446.

Rippka, R., Deruelles, J., Waterbury, J.B., Herdman, M., and Stanier, R.Y. (1979). Generic Assignments, Strain Histories and Properties of Pure Cultures of Cyanobacteria. Microbiology *111*, 1–61.

Rosenthal, P.B., and Henderson, R. (2003). Optimal determination of particle orientation, absolute hand, and contrast loss in single-particle electron cryomicroscopy. J. Mol. Biol. *333*, 721–745.

Sali, A., and Blundell, T.L. (1993). Comparative protein modelling by satisfaction of spatial restraints. J. Mol. Biol. *234*, 779–815.

Salje, J., Zuber, B., and Löwe, J. (2009). Electron cryomicroscopy of E. coli reveals filament bundles involved in plasmid DNA segregation. Science *323*, 509–512.

Saraste, M., Sibbald, P.R., and Wittinghofer, A. (1990). The P-loop–a common motif in ATP- and GTP-binding proteins. Trends Biochem. Sci. *15*, 430–434.

Saur, M., Hennig, R., Young, P., Rusitzka, K., Hellmann, N., Heidrich, J., Morgner, N., Markl, J., and Schneider, D. (2017). A Janus-Faced IM30 Ring Involved in Thylakoid Membrane Fusion Is Assembled from IM30 Tetramers. Structure *25*, 1380–1390.e5.

Schaffer, M., Engel, B.D., Laugks, T., Mahamid, J., Plitzko, J.M., and Baumeister, W. (2015). Cryo-focused ion beam sample preparation for imaging vitreous cells by cryo-electron tomography. Bio Protoc. *5*, e1575.

Schaffer, M., Mahamid, J., Engel, B.D., Laugks, T., Baumeister, W., and Plitzko, J.M. (2017). Optimized cryo-focused ion beam sample preparation aimed at in situ structural studies of membrane proteins. J. Struct. Biol. *197*, 73–82.

Scheffer, L.L., Sreetama, S.C., Sharma, N., Medikayala, S., Brown, K.J., Defour, A., and Jaiswal, J.K. (2014). Mechanism of Ca^{2+}-triggered ESCRT assembly and regulation of cell membrane repair. Nat. Commun. *5*, 5646.

Scheres, S.H.W. (2012). RELION: implementation of a Bayesian approach to cryo-EM structure determination. J. Struct. Biol. *180*, 519–530.

Schindelin, J., Arganda-Carreras, I., Frise, E., Kaynig, V., Longair, M., Pietzsch, T., Preibisch, S., Rueden, C., Saalfeld, S., Schmid, B., et al. (2012). Fiji: an open-source platform for biological-image analysis. Nat. Methods *9*, 676–682.

Schöneberg, J., Pavlin, M.R., Yan, S., Righini, M., Lee, I.-H., Carlson, L.-A., Bahrami, A.H., Goldman, D.H., Ren, X., Hummer, G., et al. (2018). ATP-dependent force generation and membrane scission by ESCRT-III and Vps4. Science *362*, 1423–1428.

Schottkowski, M., Gkalympoudis, S., Tzekova, N., Stelljes, C., Schünemann, D., Ankele, E., and Nickelsen, J. (2009). Interaction of the periplasmic PratA factor and the PsbA (D1) protein during biogenesis of photosystem II in Synechocystis sp. PCC 6803. J. Biol. Chem. *284*, 1813–1819.

Schweitzer, A., Aufderheide, A., Rudack, T., Beck, F., Pfeifer, G., Plitzko, J.M., Sakata, E., Schulten, K., Förster, F., and Baumeister, W. (2016). Structure of the human 26S proteasome at a resolution of 3.9 Å. Proc. Natl. Acad. Sci. USA *113*, 7816–7821.

Siebenaller, C., Junglas, B., Lehmann, A., Hellmann, N., and Schneider, D. (2020). Proton Leakage Is Sensed by IM30 and Activates IM30-Triggered Membrane Fusion. Int. J. Mol. Sci. *21*, 4530.

Standar, K., Mehner, D., Osadnik, H., Berthelmann, F., Hause, G., Lünsdorf, H., and Brüser, T. (2008). PspA can form large scaffolds in Escherichia coli. FEBS Lett. *582*, 3585–3589.

Stengel, A., Gügel, I.L., Hilger, D., Rengstl, B., Jung, H., and Nickelsen, J. (2012). Initial steps of photosystem II de novo assembly and preloading with manganese take place in biogenesis centers in Synechocystis. Plant Cell *24*, 660–675.

Strenkert, D., Schmollinger, S., and Schroda, M. (2013). Heat shock factor 1 counteracts epigenetic silencing of nuclear transgenes in Chlamydomonas reinhardtii. Nucleic Acids Res. *41*, 5273–5289.

Szalontai, B., Nishiyama, Y., Gombos, Z., and Murata, N. (2000). Membrane dynamics as seen by fourier transform infrared spectroscopy in a cyanobacterium, Synechocystis PCC 6803. The effects of lipid unsaturation and the protein-to-lipid ratio. Biochim. Biophys. Acta *1509*, 409–419.

Theis, J., Gupta, T.K., Klingler, J., Wan, W., Albert, S., Keller, S., Engel, B.D., and Schroda, M. (2019). VIPP1 rods engulf membranes containing phosphatidylinositol phosphates. Sci. Rep. *9*, 8725.

Theis, J., Niemeyer, J., Schmollinger, S., Ries, F., Rütgers, M., Gupta, T.K., Sommer, F., Muranaka, L.S., Venn, B., Schulz-Raffelt, M., et al. (2020). VIPP2 interacts with VIPP1 and HSP22E/F at chloroplast membranes and modulates a retrograde signal for HSP22E/F gene expression. Plant Cell Environ. *43*, 1212–1229.

Trabuco, L.G., Villa, E., Mitra, K., Frank, J., and Schulten, K. (2008). Flexible fitting of atomic structures into electron microscopy maps using molecular dynamics. Structure *16*, 673–683.

Vietri, M., Schink, K.O., Campsteijn, C., Wegner, C.S., Schultz, S.W., Christ, L., Thoresen, S.B., Brech, A., Raiborg, C., and Stenmark, H. (2015). Spastin and ESCRT-III coordinate mitotic spindle disassembly and nuclear envelope sealing. Nature *522*, 231–235.

Vothknecht, U.C., Otters, S., Hennig, R., and Schneider, D. (2012). Vipp1: a very important protein in plastids?!. J. Exp. Bot. *63*, 1699–1712.

Wagner, T., Merino, F., Stabrin, M., Moriya, T., Antoni, C., Apelbaum, A., Hagel, P., Sitsel, O., Raisch, T., Prumbaum, D., et al. (2019). SPHIRE-crYOLO is a fast and accurate fully automated particle picker for cryo-EM. Commun. Biol. *2*, 218.

Walker, J.E., Saraste, M., Runswick, M.J., and Gay, N.J. (1982). Distantly related sequences in the alpha- and beta-subunits of ATP synthase, myosin, kinases and other ATP-requiring enzymes and a common nucleotide binding fold. EMBO J. *1*, 945–951.

Weber, E., Engler, C., Gruetzner, R., Werner, S., and Marillonnet, S. (2011). A modular cloning system for standardized assembly of multigene constructs. PLoS ONE *6*, e16765.

Wehmer, M., Rudack, T., Beck, F., Aufderheide, A., Pfeifer, G., Plitzko, J.M., Förster, F., Schulten, K., Baumeister, W., and Sakata, E. (2017). Structural insights into the functional cycle of the ATPase module of the 26S proteasome. Proc. Natl. Acad. Sci. USA *114*, 1305–1310.

Westphal, S., Heins, L., Soll, J., and Vothknecht, U.C. (2001). Vipp1 deletion mutant of Synechocystis: a connection between bacterial phage shock and thylakoid biogenesis? Proc. Natl. Acad. Sci. USA *98*, 4243–4248.

Wilfling, F., Lee, C.W., Erdmann, P.S., Zheng, Y., Sherpa, D., Jentsch, S., Pfander, B., Schulman, B.A., and Baumeister, W. (2020). A Selective Autophagy Pathway for Phase-Separated Endocytic Protein Deposits. Mol. Cell *80*, 764–778.e7.

Willmund, F., Mühlhaus, T., Wojciechowska, M., and Schroda, M. (2007). The NH2-terminal domain of the chloroplast GrpE homolog CGE1 is required for dimerization and cochaperone function in vivo. J. Biol. Chem. *282*, 11317–11328.

Wolff, G., Limpens, R.W.A.L., Zheng, S., Snijder, E.J., Agard, D.A., Koster, A.J., and Bárcena, M. (2019). Mind the gap: Micro-expansion joints drastically decrease the bending of FIB-milled cryo-lamellae. J. Struct. Biol. *208*, 107389.

Zhang, K. (2016). Gctf: Real-time CTF determination and correction. J. Struct. Biol. *193*, 1–12.

Zhang, L., Kato, Y., Otters, S., Vothknecht, U.C., and Sakamoto, W. (2012). Essential role of VIPP1 in chloroplast envelope maintenance in Arabidopsis. Plant Cell *24*, 3695–3707.

Zhang, S., Shen, G., Li, Z., Golbeck, J.H., and Bryant, D.A. (2014). Vipp1 is essential for the biogenesis of Photosystem I but not thylakoid membranes in Synechococcus sp. PCC 7002. J. Biol. Chem. *289*, 15904–15914.

Zhang, L., Kondo, H., Kamikubo, H., Kataoka, M., and Sakamoto, W. (2016). VIPP1 Has a Disordered C-Terminal Tail Necessary for Protecting Photosynthetic Membranes against Stress. Plant Physiol. *171*, 1983–1995.

Zheng, S.Q., Palovcak, E., Armache, J.-P., Verba, K.A., Cheng, Y., and Agard, D.A. (2017). MotionCor2: anisotropic correction of beam-induced motion for improved cryo-electron microscopy. Nat. Methods *14*, 331–332.

Zivanov, J., Nakane, T., Forsberg, B.O., Kimanius, D., Hagen, W.J., Lindahl, E., and Scheres, S.H. (2018). New tools for automated high-resolution cryo-EM structure determination in RELION-3. eLife *7*, e42166.

Zivanov, J., Nakane, T., and Scheres, S.H.W. (2019). A Bayesian approach to beam-induced motion correction in cryo-EM single-particle analysis. IUCrJ *6*, 5–17.

STAR★METHODS

KEY RESOURCES TABLE

REAGENT or RESOURCE	SOURCE	IDENTIFIER
Antibodies		
αCurT	Heinz et al., 2016	N/A
αD1	Schottkowski et al., 2009	N/A
αVIPP1	Aseeva et al., 2007	N/A
αPsaD	Agrisera	Cat# AS09 461
αRbcL	Agrisera	Cat# AS03 037A
αPetC/αRieske	Agrisera	Cat# AS08 330
αS1	Agrisera	Cat# AS08 309
αRabbit IgG (whole molecule)–Peroxidase antibody produced in goat IgG fraction of antiserum	Sigma Aldrich	Cat# A9169
Bacterial and virus strains		
E. coli ER2566	New England Biolabs	Cat# E4130S
E. coli DH5α	ThermoFischer Scientific	Cat# 18265017
E. coli XL10-Gold	Agilent Technologies	Cat# 200314
Chemicals, peptides, and recombinant proteins		
Uranyl acetate	Serva	Cat# 77870.02
SapI	New England Biolabs	Cat# R0569L
XhoI	New England Biolabs	Cat# R0146L
BsaI	New England Biolabs	Cat# R3733L
BbsI	New England Biolabs	Cat# R0539L
EcoRV	New England Biolabs	Cat# R0195L
T4 polynucleotide kinase	New England Biolabs	Cat# M0201L
T4 DNA ligase	New England Biolabs	Cat# M0202L
Critical commercial assays		
Bradford assay using RotiQuant	Carl Roth	Cat# K015.1
ATPase assay kit	Expedeon, acquired by Abcam in Jan 2020	Cat# Expedeon: 601-0120 Abcam: ab270551
GTPase assay kit	Expedeon, acquired by Abcam in Jan 2020	Cat# Expedeon: 602-0120 Abcam: ab270553
QuikChange XL Site-Directed Mutagenesis Kit	Agilent Technologies	Cat# 200517
CloneJET PCR Cloning Kit	Thermo Fisher Scientific	Cat# K1231
Deposited data		
VIPP1 C14 structure and cryo-EM density	This paper	PDB: 7O3W, EMDB: EMD-12710
VIPP1 C15 structure and cryo-EM density	This paper	PDB: 7O3X, EMDB: EMD-12711
VIPP1 C16 structure and cryo-EM density	This paper	PDB: 7O3Y, EMDB: EMD-12712
VIPP1 C17 structure and cryo-EM density	This paper	PDB: 7O40, EMDB: EMD-12713
VIPP1 C18 structure and cryo-EM density	This paper	PDB: 7O3Z, EMDB: EMD-12714
Cryo-EM single particle raw micrograph dataset	This paper	EMPIAR: EMPIAR-10680
Cryo-electron tomogram of the *Synechocystis* wild-type VIPP1 strain grown in high light (Figure 4D)	This paper	EMDB: EMD-12324
Cryo-electron tomogram of the *Synechocystis* F4E VIPP1 mutant grown in high light (Figure 4G)	This paper	EMDB: EMD-12325

(*Continued on next page*)

Continued

REAGENT or RESOURCE	SOURCE	IDENTIFIER
Cryo-electron tomogram of the *Synechocystis* V11E VIPP1 mutant grown in high light (Figure 4J)	This paper	EMDB: EMD-12326
Cryo-electron tomogram of VIPP1-mCherry structures inside the *Chlamydomonas* chloroplast (Figures 5E and 5T)	This paper	EMDB: EMD-12327
Cryo-electron tomogram of VIPP1-mCherry structures inside the *Chlamydomonas* chloroplast (Figure 5L)	This paper	EMDB: EMD-12328
Cryo-electron tomogram of VIPP1-mCherry structures inside the *Chlamydomonas* chloroplast (No Figure)	This paper	EMDB: EMD-12329
Cryo-electron tomogram of VIPP1-mCherry structures inside the *Chlamydomonas* chloroplast (No Figure)	This paper	EMDB: EMD-12330
Crystal structure of *E. coli* PspA (amino acids 1-144)	Osadnik et al., 2015	PDB: 4WHE
Cryo-EM structure of the human 26S proteasome	Schweitzer et al., 2016	PDB: 5L4G
Cryo-EM density map of human p97 bound to the UPCDC30245 inhibitor (ADP-bound)	Banerjee et al., 2016	EMDB: EMD-3295
Cryo-EM density map of human p97 bound to ATPγS	Banerjee et al., 2016	EMDB: EMD-3299
Experimental models: organisms/strains		
Chlamydomonas reinhardtii UVM4	Neupert et al., 2009	Patented
Chlamydomonas reinhardtii UVM4 – Vipp1-mCherry	This paper	N/A
Synechocystis sp. PCC 6803 – WT, glucose tolerant	Rippka et al., 1979	N/A
Synechocystis sp. PCC 6803 – *vipp1-F4E*	This paper	N/A
Synechocystis sp. PCC 6803 – *vipp1-V11E*	This paper	N/A
Synechocystis sp. PCC 6803 – *vipp1-GFP*	Bryan et al., 2014	N/A
Oligonucleotides		
See list of primers in Table S1	This paper	N/A
Recombinant DNA		
pJET-KmR-vipp1	This paper	N/A
pJET-KmR-vipp1-F4E	This paper	N/A
pJET-KmR-vipp1-V11E	This paper	N/A
KmR-vipp1 gBloc 549 bp upstream to 47 bp downstream of the *vipp1* gene, with kanamycin resistance cassette inserted 149 bp upstream of *vipp1* (sequence taken from pBSL14; ATCC 87127)	This paper / Integrated DNA Technologies	https://www.idtdna.com/pages/products/genes-and-gene-fragments/double-stranded-dna-fragments/gblocks-gene-fragments
TYB11 (IMPACT kit)	New England Biolabs	Cat# E6901S
pAGM1287	Weber et al., 2011	N/A
pICH47742	Weber et al., 2011	N/A
pICH41766	Weber et al., 2011	N/A
pAGM4673	Weber et al., 2011	N/A
pMS451 (TYB11-*syn*VIPP1)	This paper	N/A
pMS319 (TYB11-*cr*VIPP1)	Liu et al., 2005	N/A
pMS300 (TYB11-CGE1a)	Willmund et al., 2007	N/A
pMBS478 (Level 0-*cr*VIPP1)	This paper	N/A
pCM0-020 (HSP70A-RBCS2 promoter + 5′UTR)	Crozet et al., 2018	N/A
pCM0-108 (mCherry [i1])	Crozet et al., 2018	N/A
pCM0-119 (RPL23 3′UTR)	Crozet et al., 2018	N/A
pMBS677 (Level 1-AR-*cr*VIPP1-mCherry-RPL23)	This paper	N/A
pCM1-01 (Level 1-PSAD-aadA-PSAD)	Crozet et al., 2018	N/A

(*Continued on next page*)

Continued

REAGENT or RESOURCE	SOURCE	IDENTIFIER
pMBS678 (Level 1- AR-*cr*VIPP2-mVenus-RPL23)	This paper	N/A
pMBS679 (Level 2-pCM1-01/ pMBS678/pMBS677)	This paper	N/A
Software and algorithms		
CLC Main Workbench 7.7.2	QIAGEN	https://www.qiagen.com/us/products/discovery-and-translational-research/next-generation-sequencing/informatics-and-data/analysis-and-visualization/clc-main-workbench/
Serial Cloner	Serial Basics	http://serialbasics.free.fr/Serial_Cloner.html
ImageQuant TL	GE Healthcare	http://www.cytivalifesciences.com/en/us/shop/protein-analysis/molecular-imaging-for-proteins/imaging-software/imagequant-tl-8-1-p-00110
MotionCor2	Zheng et al., 2017	https://emcore.ucsf.edu/ucsf-software
crYOLO	Wagner et al., 2019	https://cryolo.readthedocs.io/en/stable/
RELION 3.0 suite	Zivanov et al., 2018	https://www3.mrc-lmb.cam.ac.uk/relion/index.php/Main_Page
Gctf	Zhang, 2016	https://www2.mrc-lmb.cam.ac.uk/research/locally-developed-software/zhang-software/#gctf
SerialEM software	Mastronarde, 2005	https://bio3d.colorado.edu/SerialEM/
UCSF Chimera	Pettersen et al., 2004	https://www.cgl.ucsf.edu/chimera/
ChimeraX	Goddard et al., 2018	https://www.rbvi.ucsf.edu/chimerax/
Modeler software	Sali and Blundell, 1993	https://salilab.org/modeller/
Rosetta	Leaver-Fay et al., 2011	https://rosettacommons.org/home
VMD	Humphrey et al., 1996	https://www.ks.uiuc.edu/Research/vmd/
NAMD	Phillips et al., 2005	https://www.ks.uiuc.edu/Research/namd/
Biopython	Hamelryck and Manderick, 2003	https://biopython.org/
MDAnalysis	Michaud-Agrawal et al., 2011	https://www.mdanalysis.org/
GTPbinder	Chauhan et al., 2010	http://crdd.osdd.net/raghava/gtpbinder/
ATPint	Chauhan et al., 2009	http://crdd.osdd.net/raghava/atpint/
AutoDock4	Morris et al., 2009	http://autodock.scripps.edu/
LAS X software	Leica Microsystems	https://www.leica-microsystems.com/products/microscope-software/p/leica-las-x-ls/
3D Correlation Toolbox	Arnold et al., 2016	https://3dct.semper.space/
Fiji software	Schindelin et al., 2012	https://fiji.sc/
STOPGAP TOMOMAN pipeline	Khavnekar S., Wagner J., Erdmann P.S., Wan W.	https://github.com/williamnwan/TOMOMAN/
IMOD software	Kremer et al., 1996	https://bio3d.colorado.edu/imod/index.html
tom_deconv deconvolution filter	Tegunov, D.	https://github.com/dtegunov/tom_deconv/
Cryo-CARE	Buchholz et al., 2018	https://github.com/juglab/cryoCARE_T2T

(*Continued on next page*)

Continued

REAGENT or RESOURCE	SOURCE	IDENTIFIER
Amira software	FEI, Thermo Fisher Scientific	https://www.thermofisher.com/us/en/home/industrial/electron-microscopy/electron-microscopy-instruments-workflow-solutions/3d-visualization-analysis-software/amira-life-sciences-biomedical.html
TomoSegMemTV software package	Martinez-Sanchez et al., 2014	https://sites.google.com/site/3demimageprocessing/tomosegmemtv
Other		
200 mesh copper grids	Plano	Cat# G2200C
R 2/1 holey carbon-foil 200-mesh copper EM grids	Quantifoil Micro Tools	Cat# Q2100CR1
R 1/4 SiO_2-foil 200-mesh gold EM grids	Quantifoil Micro Tools	Cat# Q250AR-14S
FIB-compatible autogrids	FEI, Thermo Fisher	Cat# 1205101
Chitin resin	New England Biolabs	Cat# S6651L
Glass beads	Sigma Aldrich	Cat# G9268
Millipore concentrator (AMICON MWCO 3,000)	Merck / Millipore	Cat# UFC800396
C18 column Zorbax Eclipse Plus	Agilent	Cat# 861768-901
Agilent 1290 Infinity HPLC	Agilent	https://www.agilent.com/en/product/liquid-chromatography/hplc-systems/analytical-hplc-systems/1290-infinity-ii-lc-system
maXis II ETD mass spectrometer	Bruker	https://www.bruker.com/content/bruker/int/en/products-and-solutions/mass-spectrometry/qtof/maxis.html
Vitrobot Mark 4	FEI / Thermo Fisher Scientific	https://www.thermofisher.com/us/en/home/electron-microscopy/products/sample-preparation-equipment-em/vitrobot-system.html
Leica TCS SP8 confocal with Leica EM cryo-CLEM stage	Leica Microsystems	Prototype
Aquilos Cryo-FIB/SEM	FEI / Thermo Fisher Scientific	https://www.thermofisher.com/us/en/home/electron-microscopy/products/dualbeam-fib-sem-microscopes/aquilos-2-cryo-fib.html?SID=srch-srp-AQUILOSFIB
200 kV Tecnai F20 microscope with Eagle CCD camera	FEI / Thermo Fisher Scientific	Out of production
300 kV Titan Krios microscope	FEI / Thermo Fisher Scientific	https://www.thermofisher.com/us/en/home/electron-microscopy/products/transmission-electron-microscopes.html
K2 Summit camera with post-column energy filter	Gatan / Quantum	Out of production; http://www.blue-scientific.com/nordic-products/gatan/k2-direct-detection-camera/

RESOURCE AVAILABILITY

Lead contact

Further information and requests for resources and reagents should be directed to and will be fulfilled by the Lead Contact, Benjamin D. Engel (ben.engel@helmholtz-muenchen.de).

Materials availability

All unique/stable reagents generated in this study are available from the Lead Contact without restriction. Note that the *Chlamydomonas* VIPP1-mCherry strain was made in the patented UVM4 background (Neupert et al., 2009), and thus, may require a Materials Transfer Agreement from the authors of that study.

Data and code availability

The cryo-EM density maps for the *syn*VIPP1 rings with C14-C18 symmetries have been deposited in the Electron Microscopy Data Bank (EMDB), and the corresponding atomic models have been deposited in the Protein Data Bank (PDB), with the following accession codes: C14: PDB 7O3W, EMD-12710; C15: PDB 7O3X, EMD-12711; C16: PDB 7O3Y, EMD-12712; C17: PDB 7O40, EMD-12713; C18: PDB 7O3Z, EMD-12714. The complete single particle dataset of raw cryo-EM micrographs has been uploaded to the Electron Microscopy Public Image Archive (EMPIAR) under accession code EMPIAR-10680. *In situ* cryo-tomograms of *Synechocystis* WT, F4E, and V11E cells, as well as *Chlamydomonas* cells containing *cr*VIPP1-mCherry structures, have been deposited in the EMDB under accession codes EMD-12324 through EMD-12330. See individual tomogram descriptions in the Key Resources Table.

EXPERIMENTAL MODEL AND SUBJECT DETAILS

Synechocystis sp. PCC 6803

Synechocystis strains (WT, *vipp1-F4E*, *vipp1-V11E*, *vipp-GFP*) were grown on solid or in liquid BG11 medium (Rippka et al., 1979), at 30°C and with 30 μmol photons m^{-2} s^{-1} light in the presence of 5 mM glucose, unless stated otherwise. Liquid medium was shaken at 120 rpm. For selection of mutant strains, up to 200 μg/mL kanamycin was added to solid BG11 medium.

Chlamydomonas reinhardtii

Chlamydomonas VIPP1-mCherry cells were grown on solid or in liquid Tris-acetate-phosphate (TAP) medium, at room temperature and with 40 μmol photons $m^{-2}s^{-1}$ light, unless stated otherwise. Liquid medium was shaken at 120 rpm. For selection of transformants, 100 μg/mL spectinomycin was added to solid TAP media.

Generation of *Synechocystis* mutant strains

To create the *Synechocystis* mutants as well as a control strain, a construct was designed containing the *vipp1* gene with its flanking non-coding regions up to 549 bp upstream and 47 bp downstream of the *vipp1* gene. A kanamycin resistance cassette (sequence taken from pBSL14 (ATCC 87127)) was inserted 149 bp upstream of *vipp1*. The construct was ordered as a gBlock DNA fragment (Integrated DNA Technologies), blunt-cloned in the pJET1.2 vector (Thermo Fisher Scientific) and subsequently subjected to site-directed mutagenesis (QuikChange XL Site-Directed Mutagenesis Kit, Agilent Technologies) according to manufacturer's instructions to introduce the mutations F4E or V11E (primer pairs: vipp1-F4E-for + vipp1-F4E-rev, vipp1-V11E-for + vipp1-V11E-rev; Table S1). The sequences of both mutant constructs as well as the control construct were verified by sequencing, and the constructs were transformed into *Synechocystis* wild-type cells as previously described (Eaton-Rye, 2004). Complete segregation of the resulting control and mutant strains was verified by PCR (primers vipp1-seq-for + vipp1-seq-rev; Table S1), and the insertion of the mutations during homologous recombination was confirmed again by sequencing (primer vipp1-seq-rev).

Cloning of the VIPP1-mCherry construct and transformation into *Chlamydomonas*

The *VIPP1* genomic sequence, including all seven introns, was modified at positions C411G, C414T, G417C, and T420C relative to the ATG start codon to change to synonymous codons but render the sequence insensitive to attack by the siRNA produced by *VIPP1*-amiRNA construct pMS552 (Nordhues et al., 2012). Moreover, position C583G was modified to create a synonymous codon that removed a BbsI recognition site. The sequence was flanked with BbsI cleavage sites, which upon BbsI digestion yielded a 2786-bp fragment with AATG and TTCG overhangs for the B3/4 position of level 0 parts according to the Modular Cloning (MoClo) syntax for plant genes (Weber et al., 2011; Patron et al., 2015). Synthesis of the sequence and cloning into the pAGM1287 vector was performed by DC Biosciences Ltd. (Scotland), giving rise to pMBS478. This level 0 part was then complemented with level 0 parts (pCM) from the *Chlamydomonas* MoClo toolkit (Crozet et al., 2018) to fill the respective positions in level 1 modules as follows: A1-B2 – pCM0-020 (*HSP70A-RBCS2* promoter + 5′UTR); B5 – pCM0-108 (mCherry (i1)); B6 – pCM0-119 (RPL23 3′UTR). The *HSP70A-RBCS2* fusion promoter contains 467 bp of sequence upstream of the *HSP70A* start codon in optimal spacing with respect to the *RBCS2* promoter (Lodha et al., 2008; Strenkert et al., 2013). The level 0 parts and destination vector pICH47742 (Weber et al., 2011) were combined with BsaI and T4 DNA ligase and directionally assembled into level 1 module pMBS677. The latter was then combined with pCM1-01 (level 1 module with the *aadA* gene conferring resistance to spectinomycin) from the *Chlamydomonas*

MoClo kit, with plasmid pMBS678 containing the *VIPP2* gene fused to mVenus, with plasmid pICH41766 containing the proper end-linker, and with destination vector pAGM4673 (Weber et al., 2011), digested with BbsI, and ligated to yield level 2 device pMBS679. 1 μg DNA of construct pMBS679 was linearized with EcoRV and transformed into *Chlamydomonas* strain UVM4 (Neupert et al., 2009) using the glass beads method (Kindle, 1990). Transformants were selected on 100 μg/mL spectinomycin.

METHOD DETAILS

*syn*VIPP1 and *cr*VIPP1 vector design, protein expression and purification

The region coding for wild-type *syn*VIPP1 was amplified from *Synechocystis* genomic DNA using primers VIPP1-SpeI-SapI and VIPP1-XhoI (Table S1). The 839-bp PCR product was digested with SapI and XhoI and ligated into SapI–XhoI-digested pTYB11 (NEB), generating pMS451. The region coding for wild-type *cr*VIPP1 was cloned into pTYB11 (pMS319) previously (Liu et al., 2005). Single mutations were introduced by PCR (30 s at 98°C, 20 s at 63-70°C, 7.5 min at 72°C) using the primer pairs given in Table S1 and pMS451 or pMS319 as templates. For the *syn*VIPP1 E126Q+E179Q double mutant, the plasmid harboring the E126Q mutant was used as a template. PCR products were phosphorylated with polynucleotide kinase (NEB) and circularized with T4 DNA ligase (NEB). Correct cloning was verified by Sanger sequencing. All *syn*VIPP1 and *cr*VIPP1 variants and the CGE1a protein (pMS300) (Willmund et al., 2007) were produced in *E. coli* ER2566 as C-terminal fusions to a chitin-binding domain/intein and purified by chitin-affinity chromatography. For this, a 10 mL overnight culture was diluted into 1 L TB containing 100 μg/mL ampicillin and grown at 37°C for 7-8 h. IPTG was then added to a final concentration of 0.5 mM, and growth continued at 18°C overnight. Cells were harvested by centrifugation at 5,000 g and 4°C for 10 min, resuspended in 25 mL ice-cold lysis buffer (20 mM HEPES-KOH pH 8.0, 0.5 M NaCl, 1 mM EDTA, 0.1% Triton X-100, Roche cOmplete^{TM} EDTA-free protease inhibitor cocktail) and sonicated. After centrifugation at 20,000 g and 4°C for 30 min, the supernatant was passed twice at a flow rate of 0.5 mL/min through a column with 6 mL chitin beads (NEB) equilibrated with lysis buffer. The column was then washed with 100 mL lysis buffer at 2 mL/min, followed by a wash with 10 mL KMH buffer (20 mM HEPES-KOH pH 7.6, 80 mM KCl, 2.5 mM $MgCl_2$) containing 5 mM ATP to remove DnaK binding to VIPP1. For the GTP-exchange mass spectrometry experiment (Figure 2F), an additional wash was performed with 5 mM GTP in 10 mL KMH buffer. After a final wash with 20 mL lysis buffer lacking Triton at 2 mL/min, the column was flushed with 10 mL cleavage buffer (20 mM Tris-HCl pH 9.0, 0.5 M NaCl, 1 mM EDTA, 50 mM DTT), gently agitated overnight at room temperature, and the recombinant protein slowly eluted. Elution was finalized with 5 mL KMH buffer to yield ~10 mL of eluate, which was then concentrated to 1–2 mL by centrifugation at 4500 g using a Millipore concentrator (AMICON MWCO 3,000). The concentrate was diluted with 20 mL buffer and reconcentated back to 1–2 mL four times: twice with dialysis buffer 1 (20 mM Tris-HCl, pH 7.5, 200 mM NaCl, 75 mM NaSCN) and then twice more with dialysis buffer 2 (20 mM Tris-HCl, pH 7.5, 50 mM NaCl, 75 mM NaSCN). After the final run, the protein concentration was determined using the Bradford assay. The purity of the protein preps was confirmed by SDS-PAGE followed by Coomassie stain (Figure S1A). Proteins were either kept on ice for analysis by cryo-EM, or quick-frozen in liquid nitrogen and stored at –80°C.

Negative-stain EM data acquisition

5 μL of purified *syn*VIPP1 protein was applied to glow discharged, 200 mesh copper grids (G2200C, Plano GmbH) that had been coated with homemade carbon film. The sample was incubated for 2 min, blotted, washed three times with water, and then stained with 2% uranyl acetate for 30 s. Images were recorded using a Tecnai F20 FEG microscope (FEI, Thermo Fisher Scientific) operated at 200 kV, with an FEI Eagle CCD camera, a calibrated pixel size of 2.21 Å, and a defocus range of −2 to −5 μm.

Cryo-EM data acquisition

Cryo-EM grids were prepared with freshly purified *syn*VIPP1 protein at a concentation of 1–2 mg/mL. 4 μL of the protein was applied to glow discharged, holey carbon-coated copper grids (R 2/1, 200 mesh, Quantifoil Micro Tools). Grids were plunge-frozen in a liquid ethane/propane mixture using a Vitrobot Mark 4 (FEI, Thermo Fisher Scientific). Blotting chamber conditions were set to 4 °C and 95% humidity, and grids were blotted using blot force 10 and a blot time of 10 sec. Grids were stored in liquid nitrogen until usage. Images were acquired on a Titan Krios microscope (FEI, Thermo Fisher Scientific) at 300 kV, using a post-column energy filter (Quantum, Gatan) and a K2 Summit direct electron detector (Gatan) operated in counting mode. For each image, 80 frames were acquired over 8 s, with a total dose of ~45 $e^-/Å^2$. A total of 8120 images were recorded, using a calibrated pixel size of 1.35 Å and a defocus range of −0.5 to −3.5 μm.

Cryo-EM image processing and single particle analysis

See the workflow in Methods S1. The frame stacks were subjected to alignment with 5x5 patches and dose filtering using MotionCor2 (Zheng et al., 2017), yielding 8120 aligned and dose-weighted micrograph images (Figure S1B, Methods S1A). Automated particle picking was performed with crYOLO (Wagner et al., 2019) by training on a small dataset of 80 manually-picked images and then using this trained network to pick particles from the full dataset. All subsequent image processing was carried out using the RELION 3.0 software suite (Zivanov et al., 2018). CTF parameters were determined using Gctf (Zhang, 2016). Based on the crYOLO picking, ~337,000 particles were extracted (defined as Dataset-A). After particle extraction, the dataset was cleaned using reference-free 2D classification (Figure S1C), yielding ~263,000 particles (defined as Dataset-B).

To generate a reference-free initial 3D model, we used a RELION implementation of stochastic gradient descent (SGD) (Punjani et al., 2017) without applying symmetry (Methods S1B). The SGD algorithm allows for *ab initio* heterogeneous structure determination without a prior reference map. Starting with Dataset-B, a very rough class was obtained from ~33,000 particles. Another round of SGD was performed using these particles, and ~20,000 particles were selected to produce an improved 3D map exhibiting C17 symmetry. Using this volume as a reference, 3D classification of the ~20,000 particles was performed without applying symmetry constraints. The 3D classification split the particles into several classes, yielding 3D maps for both C15 and C17 symmetries. Using these two volumes as references, a new 3D classification of the full Dataset-B was performed, while enforcing symmetry constraints (Methods S1C). This split the particles into two large classes (C15 and C17) and generated improved 3D maps to be used as references for the next round of 3D classification. To obtain homogeneous classes of particles, ~120,000 particles from the C15 class and ~62,000 particles from the C17 class were subjected to several rounds of 3D classification (Methods S1D). These classifications split the particles into new classes with C14, C15, C16, C17 and C18 symmetries. Several rounds of 3D refinement were performed for these symmetry classes, yielding 3D structures with resolutions ranging from 4.5 Å to 6.5 Å (Methods S1E).

When further rounds of 3D classification and refinement did not improve the resolution of Dataset-B, the final density maps of each symmetry were used as references for 3D classification of the full Dataset-A (~337,000 particles) (Methods S1F and S1G). The reason behind this was to extract the particles directly from the initial dataset based on the specific 3D references corresponding to each symmetry class. Coarse angular sampling (7.5°) was applied to speed up the classification process, and the dataset was divided into five classes corresponding to specific symmetries (Methods S1F). Each symmetry class was then subjected to several rounds of 3D classification with fine angular sampling (3.5°) (Methods S1G). The goal of this step was to clean the classes further, increasing the structural homogeneity of the particles.

The final classes were next processed through iterative rounds of RELION 3D auto-refinement to improve the alignment (Scheres, 2012), per-particle CTF refinement to estimate the defocus and astigmatism of each particle (Zivanov et al., 2018), and Bayesian polishing to correct for the motion of each particle (using frames 3-50) and filter for the radiation damage (Zivanov et al., 2019; Methods S1H and S1I). Alignment was carried out following the "gold-standard" procedure, which randomly splits the dataset into two half sets and aligns them independently. This allowed calculation of a Fourier shell correlation (FSC) curve for resolution estimation (Figure S1E) using the FSC = 0.143 threshold criterion (Rosenthal and Henderson, 2003). Local resolution maps (Figure S1F) were generated with the RELION local resolution function (Cardone et al., 2013). The Cryo-EM map and molecular model statistics are listed in Methods S1J. Images of the cryo-EM density maps were generated with UCSF Chimera (Pettersen et al., 2004) and ChimeraX (Goddard et al., 2018).

Modeling of VIPP1 into the cryo-EM density

The initial PDB structure of *syn*VIPP1 was obtained by homology modeling with Modeler software (Sali and Blundell, 1993) starting with the available crystal structure of *E. coli* PspA (PDB: 4WHE, corresponding to helices H2 and H3 of VIPP1) (Osadnik et al., 2015) and the *syn*VIPP1 sequence (UniProt: A0A068MW27). Domains not resolved in the crystal structure (residues 2-25 and 142-216, corresponding to helices H1, H4/5, and H6) were modeled using the Rosetta (Leaver-Fay et al., 2011) *ab initio* structure prediction framework implemented as a plugin in VMD software (Humphrey et al., 1996). This framework was initially developed to furnish the structurally unresolved regions of the 26S proteasome (Schweitzer et al., 2016). We did not model the VIPP1 C terminus (residues 217-267, corresponding to H7 and a disordered linker), as it was not resolved within the EM density map, presumably due to its highly dynamic nature (Figures 1F and 1G). The models were clustered using the k-means algorithm. For each symmetry, single subunits for each layer of the VIPP1 ring were segmented.

Each of the clusters obtained was fitted into the segmented maps using molecular dynamics flexible fitting (MDFF) (Trabuco et al., 2008). MDFF employs molecular dynamics to fit initial models into a density in real space, and thus, permits protein flexibility while maintaining realistic protein conformations (Goh et al., 2016). We used NAMD (Phillips et al., 2005) with the CHARMM36 force field for MDFF calculations. During MDFF runs, restraints to preserve the secondary structure, chirality, and cis-peptide bonds were applied to avoid overfitting. As further step to reduce artifacts due to overfitting, all MDFF runs were performed at a modest gscale of 0.3.

After MDFF convergence, the cross-correlation coefficient for the clusters was calculated, and the structure showing the highest correlation was used for subsequent steps. Once subunits for each segment were fitted by interactive MDFF, the entire structure was created by applying the respective symmetry operation (C14, C15, C16, C17, and C18) on the model. The whole structure was then refined using MDFF and symmetry-adapted constraints to apply a harmonic potential to the symmetry-averaged positions of each individual VIPP1 subunit within the complete ring. After this refinement, the structures were re-symmetrized with Biopython (Hamelryck and Manderick, 2003) using six selected monomers, one from each layer of the VIPP1 ring. Steric clashes between the symmetry subunits were removed by MDFF energy minimization of the whole structure into the cryo-EM density map. The interaction network between VIPP1 monomers in the ring (Figure S2D) was generated using MDAnalysis (Michaud-Agrawal et al., 2011) based on the distances between residues within the VIPP1 structure.

The initial prediction of a nucleotide binding site in *syn*VIPP1 was performed using the GTPbinder (Chauhan et al., 2010) and ATPint (Chauhan et al., 2009) web servers. AutoDock4 (Morris et al., 2009) was used to predict possible nucleotide binding modes. We aligned the ADP from the human 26S proteasome structure (PDB: 5L4G) (Schweitzer et al., 2016) with the best scoring result. The model of the nucleotide binding region was further refined to the density in real space by an iterative combination of MDFF with *ab initio* structure prediction as well as Monte Carlo-based backbone and side-chain rotamer search algorithms, following the

strategy detailed in Wehmer et al. (2017). Subsequently, we further refined the nucleotide binding pocket using interactive MDFF to manually pull side chains into EM density, while interactively checking the cross-correlation values in VMD.

Finally, the complete structure was refined with Phenix software (Liebschner et al., 2019) real space refinement with reference coordinate restraints (σ = 0.05) on the nucleotide binding site. The resulting structure was re-symmetrized.

Detection of VIPP1-bound nucleotide by mass spectrometry

The ATP and GTP wash steps were performed during purification while the VIPP1 protein was bound to the chitin column, as described above. Purified VIPP1 at a concentration of 1 μM was injected onto a C18 column (Agilent Zorbax Eclipse Plus C18, 2.1 × 100 mm^2, pore size 3.5 μm), mounted on an Agilent 1290 HPLC apparatus. Bound ligands were eluted at 250 μL/min using a gradient of buffer A (20 mM triethylammonium acetate (pH 9.0)) and buffer B (20 mM triethylammonium acetate (pH 9.0), 20% acetonitrile) as previously described (Gat et al., 2019). The experiment was conducted at pH 9.0, with the mass spectrometer (maXis II ETD, Bruker) operating in negative ion mode, with a mass range of 200–1,200 m/z and collision cell energy of −10.0 eV to accommodate detection of the negatively charged compounds. Therefore, the masses of both ADP and GDP are off by −1 Da (Figures 2F, S4A, and S4B).

VIPP1 nucleotide hydrolysis assays

ATP and GTP hydrolysis assays were carried out as previously described (Ohnishi et al., 2018) with slight modifications, using ATPase and GTPase assay kits (Expedeon Ltd.) that employ a malachite green-based detection system with PiColorLock™. All reactions were performed in a 200 μL volume according to the manufacturer instructions. The reaction mixture contained 50 mM Tris-HCl (pH 7.5), 2.5 mM $MgCl_2$, 0.5 mM ATP or GTP, and purified *syn*VIPP1 or *cr*VIPP1 recombinant protein. The ATP hydrolysis assay was performed with 12 μg of recombinant protein, whereas the GTP hydrolysis assay was performed with either 6 μg of *syn*VIPP1 or 4 μg of *cr*VIPP1 protein. Reaction mixtures were incubated at 37°C for 30 min and were then immediately cooled in ice water for 1 min. Subsequently, each reaction was terminated by adding 50 μL of PiColorLock™ at room temperature. Unless specifically described, the 30 min incubation time was used as the standard condition. The released Pi in each reaction mixture was quantified by measuring absorption at 635 nm according to the calibration curve obtained from the absorption of Pi standard solutions (see Figure S4C). Because stock solutions of ATP and GTP always contain a trace amount of free Pi, measurements were normalized by the background absorption value of reaction mixture that had not been supplemented with recombinant protein to obtain VIPP1-dependent Pi release.

Physiological and biochemical analysis of *Synechocystis* mutants

For growth analysis, log-phase *Synechocystis* cultures grown in low light (30 μmol photons m^{-2} s^{-1}) were adjusted to OD_{750} = 1 and dilution series were prepared up to OD_{750} = 10^{-4}. Next, 5 μl of each dilution and strain were spotted on solid BG11 with and without glucose. Plates were incubated in low light and high light (200 μmol photons m^{-2} s^{-1}) and the results were documented after 5 days of growth.

For analysis of whole cell protein accumulation, *Synechocystis* pre-cultures were grown in low light for 2 days until they reached log phase. Main cultures were inoculated to OD_{750} = 0.1 and grown in low light or high light for 24 h. Cells were harvested by centrifugation, resuspended (50 mM Tris-HCl pH 7, 20 mM $MgCl_2$, 20 mM KCl, 0.5% Triton X-100) and broken using a BeadBug Homogenizer (Biozym) and glass beads in three cycles of alternating 20 s shaking and 1 min incubation on ice. Lysates were incubated on ice for 15 min, centrifuged (20,000 g, 1 min 4°C) and the supernatant protein concentrations were determined by Bradford assay using RotiQuant (Carl Roth GmbH + Co. KG). Samples were subjected to western blot analysis, and quantification of the results from three independent biological replicates was performed using the ImageQuant TL software (GE Healthcare). Generation of the antibodies used in this study has been described previously: αCurT (Heinz et al., 2016), αD1 (Schottkowski et al., 2009) and αVIPP1 (Aseeva et al., 2007). Additional antibodies were purchased from Agrisera: αPsaD, αRbcL, αRieske and αS1.

Synechocystis vitrification, cryo-FIB milling, and cryo-ET data acquisition

Growth of *Synechocystis* WT, *vipp1-F4E*, and *vipp1-V11E* strains for *in situ* cryo-ET was performed identically as described above for physiological and biochemical analysis. The *vipp1-GFP* strain was grown at 8 μmol photons $m^{-2}s^{-1}$ for the very low light condition and transferred to 600 μmol photons $m^{-2}s^{-1}$ for 1 h for the very high light condition, as described in Bryan et al. (2014). Using a Vitrobot Mark 4 (FEI, Thermo Fisher Scientific), 4 μL of cell culture was blotted onto R 1/4 SiO_2-foil 200-mesh gold EM grids (Quantifoil Micro Tools) and plunge frozen in a liquid ethane/propane mixture. Grids were stored in liquid nitrogen until used for FIB milling. Cryo-FIB milling was performed essentially as previously described (Schaffer et al., 2015, 2017), using an Aquilos dual-beam FIB/SEM instrument (FEI, Thermo Fisher Scientific). Grids were clipped into Autogrid support rings modified with a cut-out that allows access to the ion beam at low angle (FEI, Thermo Fisher Scientific). In the FIB/SEM chamber, the grids were sputter-coated with metallic platinum to reduce charging, then coated with a thicker layer of organometallic platinum using a gas injection system to protect the sample surface. Micro-expansion joints (relief cuts) were milled to release stress in the support film and help prevent lamella bending (Wolff et al., 2019). The cells were then milled with a gallium ion beam to produce lamellae of 100-200 nm thickness, and the grids were transferred out of the FIB/SEM and stored in liquid nitrogen until imaged by cryo-ET.

Grids containing milled samples were transferred into a 300 kV Titan Krios microscope (FEI Thermo Fisher), equipped with a post-column energy filter (Quantum, Gatan), and a direct detector camera (K2 summit, Gatan). Using SerialEM software (Mastronarde, 2005), dose-symmetric tilt-series were acquired (Hagen et al., 2017), starting at +10° to match the pre-tilt of the lamella and then proceeding with 2° steps to roughly −50° and +70°. Individual tilts were recorded in movie mode with 10 frames per second, at an object pixel size of 3.52 Å and a target defocus of −4 to −5.5 μm. The total accumulated dose deposited on each tilt-series ranged from 90 to 140 e-/Å^2.

Chlamydomonas vitrification and cryo-CLEM workflow

Chlamydomonas VIPP1-mCherry cells were grown until mid-log phase in TAP media, shaking at 120 rpm with 40 μmol photons $m^{-2}s^{-1}$ light. Vitrification was performed as described above for *Synechocystis*, except that cells were frozen onto R 1/2 carbon-foil 200-mesh copper EM grids (Quantifoil Micro Tools). Grids were clipped into FIB-compatible Autogrid support rings (FEI, Thermo Fisher Scientific) and transferred into a Leica TCS SP8 confocal microscope equipped with a Leica EM cryo-CLEM stage and transfer system (Leica Microsystems). Imaging was performed with an HC PL APO 50x/0.90 DRY objective in transmitted light and fluorescence modes using 552 nm laser excitation (OPS) at 0.6% intensity (corresponding to ~0.033 mW) with a pinhole size of 0.90 and two detection channels: 610-633 nm for mCherry and 710-720 nm for chlorophyll autofluorescence. The field of view was adjusted to the size of individual grid squares for subsequent correlative targeting. To account for the *Chlamydomonas* cell size, ~10 um z stacks with a z-spacing optimized for the pinhole were acquired at each selected position using LAS X software (Leica Microsystems). Z-stack images were deconvolved using Huygens Essential software (Scientific Volume Imaging). Cryo-FIB milling was performed as described above. Areas of interest were targeted based on the fiducial and landmark coordinates obtained from z stacks using the 3D Correlation Toolbox (Arnold et al., 2016) and Fiji software (Schindelin et al., 2012). After transferring grids to the Titan Krios, low-magnification overviews of the lamellae were acquired with tiled montages at 6500x magnification to enable precise targeting of the VIPP1-mCherry puncta for cryo-ET. Figure 6 shows examples of correlative overlays between the Leica confocal (Figures 6A and 6H) and Aquilos SEM overviews (Figures 6B and 6I), as well as correlation of the same fluorescence images with the Titan Krios TEM overviews (Figures 6C, 6D, 6J, and 6K). Tilt-series were acquired as described above.

In situ cryo-ET reconstruction, denoising, and segmentation

The tilt-series were preprocessed and assembled with the STOPGAP TOMOMAN pipeline (https://github.com/williamnwan/TOMOMAN/), including drift correction of raw frames with MotionCor2 software (Zheng et al., 2017) and dose-weighting of individual tilts. Using IMOD software (Kremer et al., 1996), the assembled tilt-series were aligned with patch tracking, and bin4 tomographic volumes (14.08 Å pixel size) were reconstructed by weighted back projection. To enhance contrast for display, we applied the tom_deconv deconvolution filter (https://github.com/dtegunov/tom_deconv) to the bin4 *Synechocystis* tomograms (with the exception of those in Figure S8) and the Cryo-CARE denoising filter (Buchholz et al., 2018) to the bin4 *Chlamydomonas* tomograms. Slices through tomogram volumes (Figures 4, 5, 6, S6, S7, and S8) were generated with the IMOD 3dmod viewer. Tomogram segmentation was performed in Amira software (FEI, Thermo Fisher Scientific), using a combination of manual segmentation and automated membrane detection from the TomoSegMemTV software package (Martinez-Sanchez et al., 2014).

QUANTIFICATION AND STATISTICAL ANALYSIS

Estimation of the distribution of rings and rods in *syn*VIPP1 mutant proteins

The single mutations we inserted into N-terminal H1 caused some *syn*VIPP1 proteins to assemble into rods instead of rings *in vitro*. We performed a grid-based measurement of negative-stain EM images to roughly estimate the percentage of VIPP1 protein incorporated within rings and rods for each of the mutants (Figure S5). The dimensions of the negative-stain micrographs were 4096x4096 pixels, with a pixel size of 0.221 nm. Therefore, each micrograph was a square with a side length of 905 nm. Based on the dimensions of VIPP1 rings and rods (30-40 nm diameter), a grid spacing of 100 nm was chosen, yielding a grid map of 8x8 squares. The 8x8 grid map was overlaid on each of the images, and the presence of rings and/or rods in each square was manually counted. For both rings and rods, if more than ~25% of a structure was contained within a grid square, that square was counted. Rods frequently extended through several squares, resulting in multiple counts for one structure. Thus, the goal of this analysis was not to measure the relative abundance of ring and rod structures, but rather to estimate the percentage of VIPP1 protein incorporated into the two types of structures. The cumulative results are shown in Figure 3F. For each plotted bar in the graph, we analyzed 20-50 images from 2-3 grids, produced from 2-4 independent protein preps.

In situ cryo-ET measurements

For thylakoid measurements (Figure 4L), 2D slices (zoomed 6x with interpolation) were generated from the bin4 tomographic volumes using the IMOD 3dmod viewer. The slices were oriented with the xy-plane perpendicular to the thylakoid membranes (i.e., the thylakoids were viewed in cross-section). Using Fiji software (Schindelin et al., 2012), line scan intensity profiles were generated with a 40 pixel-wide line (9.4 nm) drawn perpendicular to the thylakoid sheet. Lumen width was measured between the shoulders of the peaks corresponding to opposing lipid bilayers of each thylakoid (see Engel et al., 2015). The measurement point on the peak shoulder was defined as the halfway point between the dark peak of the EM density and the adjacent light peak of the fringe caused by the contrast

transfer function. Similarly, membrane thickness was estimated by measuring the width of the peak corresponding to each bilayer (from shoulder to shoulder). A total of 50 tomograms were reconstructed, from which 48 were used for the analysis (WT: 7 LL and 6 HL; F4E mutant: 12 LL and 9 HL; V11E mutant: 7 LL and 7 HL). A total of 283 thylakoid membrane regions were used to generate 346 line scans (WT: 37 scans on 26 LL thylakoids and 28 scans on 25 HL thylakoids; F4E: 87 scans on 71 LL thylakoids and 63 scans on 52 HL thylakoids; V11E: 63 scans on 51 LL thylakoids and 68 scans on 58 HL thylakoids). For each thylakoid, scans were performed at the widest region and not more than once per 500 nm of thylakoid length. Line scan intensity profiles of putative *syn*VIPP1 and *syn*-VIPP1-GFP (Figure S8E) were generated in a similar manner, using 2D slices (zoomed 4x with interpolation) from bin4 tomograms and a 15 pixel-wide line (5.3 nm) drawn perpendicular to the wall of the structure. For both WT *syn*VIPP1 (gray in Figure S8E) and *syn*-VIPP1-GFP (green in Figure S8E), 15 individual line scans were aligned with each other using the middle peak, which corresponds to putative VIPP1. This caused the averages of the membrane bilayer and putative GFP peak to be slightly broader due to variable positioning of these peaks relative to the central VIPP1 peak.

Supplemental figures

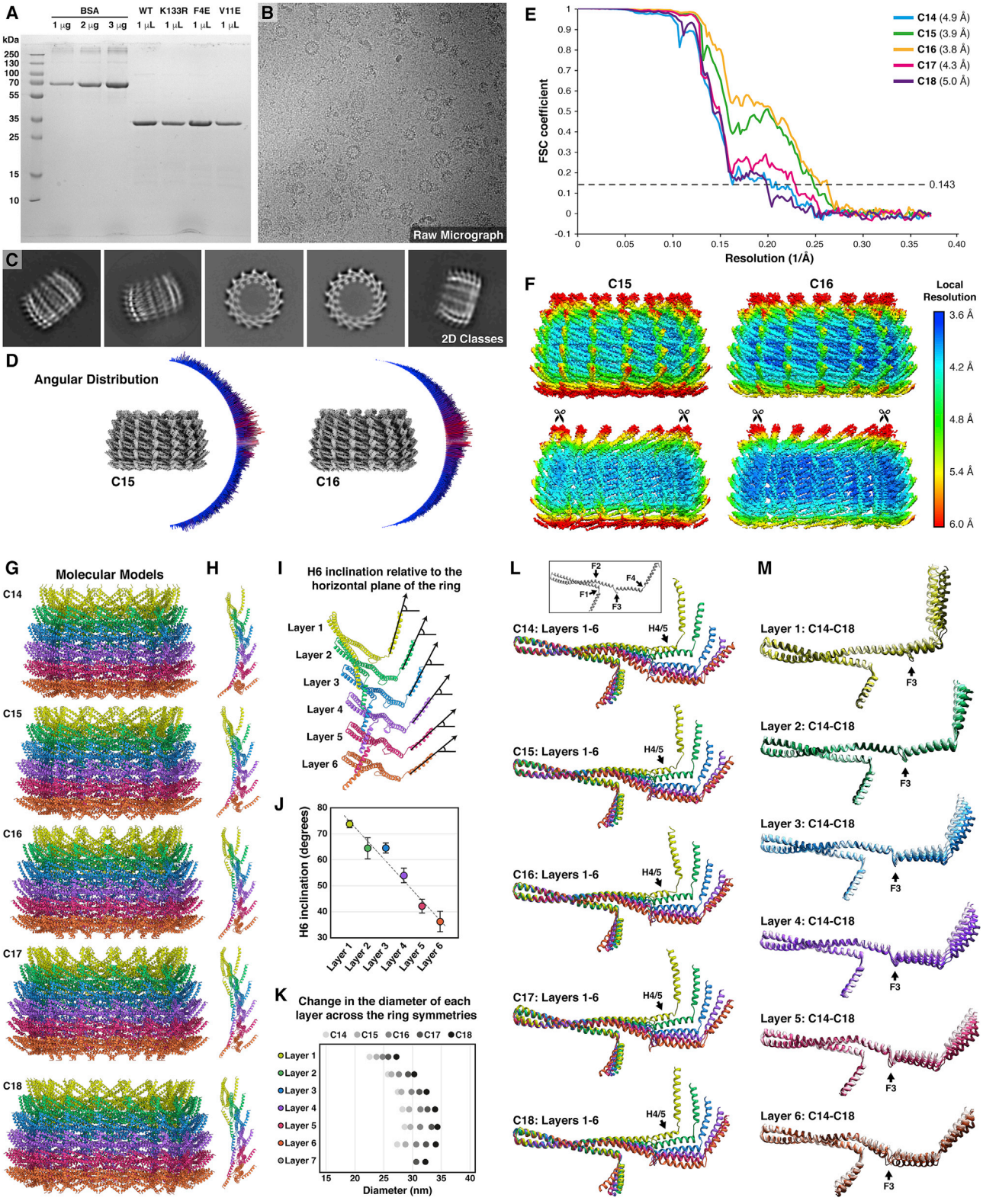

(legend on next page)

Figure S1. *syn*VIPP1 protein purification, cryo-EM processing, resolution estimation, molecular modeling, and analysis of monomer flexibility across ring layers and symmetries, related to Figure 1

(A) Coomassie-stained SDS-PAGE of four different *syn*VIPP1 preparations, run along with BSA protein concentration standards and a molecular mass ladder. VIPP1 has a molecular mass of ~29 kDa. (B) Example raw micrograph containing top and side views of *syn*VIPP1 particles. (C) Representative reference-free 2D class averages, showing side and top views. (D) Angular distribution of particles in the final C15 and C16 averages. More populated side views are red. Less populated oblique and top views are blue. (E) "Gold-standard" Fourier shell correlation (FSC) plots for the five VIPP1 ring structures (C14-C18). Numerical resolution values were determined with the FSC = 0.143 cutoff (dashed line). (F) Local resolution of the C15 and C16 maps, estimated in RELION with the local resolution function and plotted in UCSF Chimera. All structures are displayed from the side, with the top panels showing the outside surfaces of the rings and the bottom panels showing cut-open views of the rings that reveal the H1 helices. (G) Molecular models for five different symmetries of VIPP1 rings. The color scheme matches Figure 1. Although density maps for the C17 and C18 rings show seven layers (Figure 1H), only the first six layers from the top could be modeled due to the low resolution of layer 7. (H) One vertical row of monomers is displayed, showing the inclination of H1 (left side) and H6 (right side) for each ring structure. (I) For each VIPP1 structure, the inclination of H6 was measured as the angle relative to the horizontal plane of the ring. (J) Plot of the mean H6 inclination (dot) and standard deviation (error bars) from all symmetries. (K) Plot showing the diameter of each layer for each symmetry. Diameters were measured from the outer walls of the cryo-EM maps. (L, inset) VIPP1 monomers have four regions of flexibility (F1-F4). (L) All four regions flex to build a ring: VIPP1 monomers from each layer superimposed for rings of each symmetry. In layer 1, part of H4/5 is remodeled into a coil (see Figure S3B–S3D). (M) Only F3 flexes to accommodate different symmetries: superposition of VIPP1 monomers from the same layers across all five symmetries (five shades of color, with C14 the darkest and C18 the lightest).

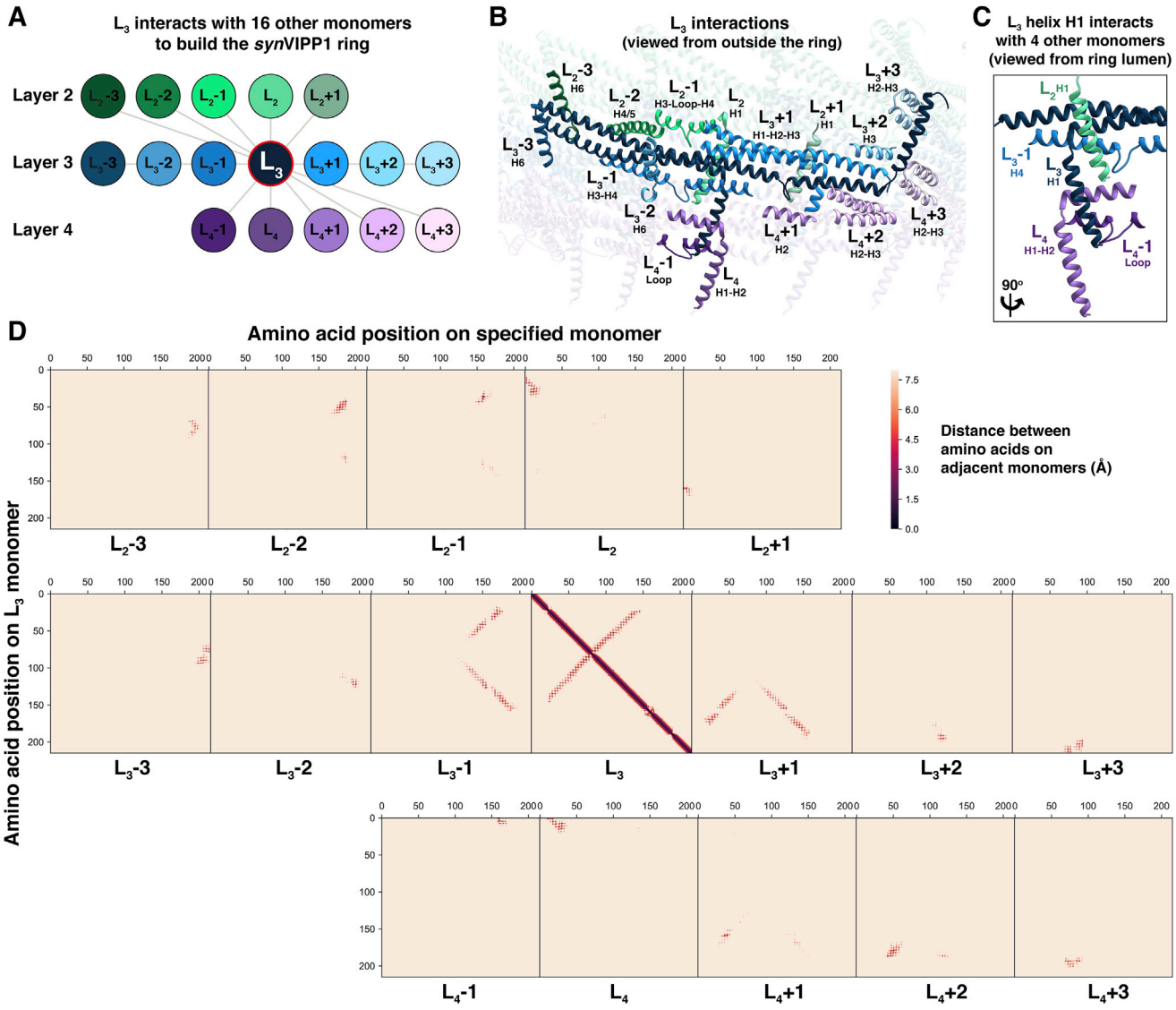

Figure S2. Network of interactions for one monomer in the VIPP1 ring, related to Figure 1

(A) Interaction schematic for one VIPP1 monomer from layer 3 (L_3, dark blue). The numbering of neighbor proteins is assigned with respect to L_3: monomers that are positioned to the right of L_3 are labeled +1, +2, and +3, whereas monomers that are positioned to the left of L_3 are labeled −1, −2, and −3. Monomers that are directly above and below L_3 are labeled L_2 and L_4, as these monomers come from layer 2 and layer 4, respectively. (B) Domains of the neighboring monomers that are in close proximity and can interact with the L_3 reference monomer. (C) The N-terminal H1 interacts with four other VIPP1 monomers: one monomer from the layer above (layer 2, in this case), one monomer from within the same layer (layer 3, in this case) and two monomers from the layer below (layer 4, in this case). (D) Interaction map for the L_3 monomer. Each square plots the shortest distance between each amino acid residue in the L_3 monomer (y axis) to each amino acid in an adjacent monomer from layers 2, 3, and 4 (x axis). Distances are color-coded according to the scale bar, with red colors indicating distances < 6 Å. Patches of red represent interaction interfaces between the monomers. The solid diagonal line from the top left to the bottom right of the central L_3 x L_3 square is autocorrelation. The second, lighter diagonal line in this square is the hairpin coiled-coil interaction between the VIPP1 monomer's H2 and H3 domains (see Figure 1G). In total, one VIPP1 monomer can interact with up to 16 neighbors.

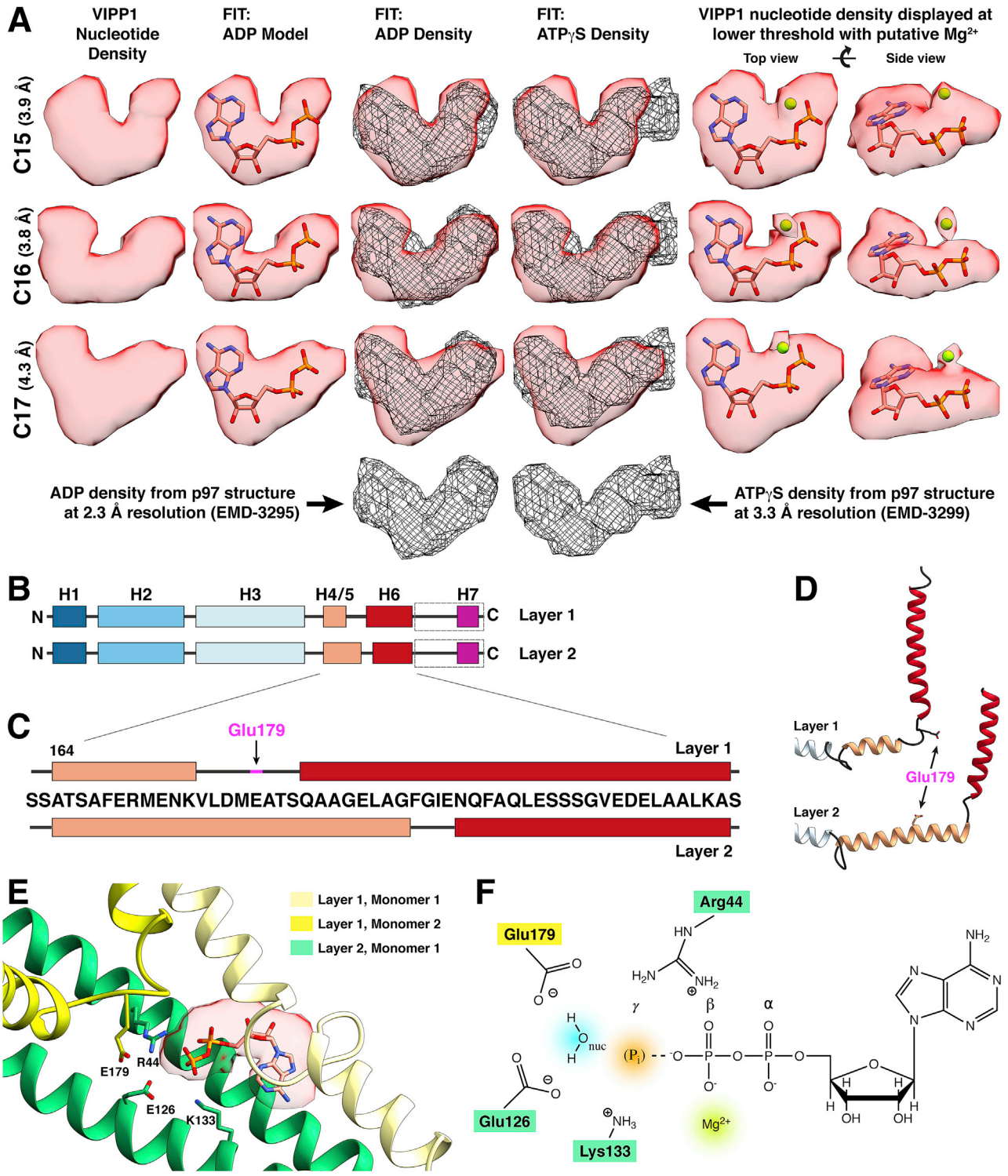

Figure S3. Analysis of the VIPP1 nucleotide density and detail of how the helix-to-coil transition in layer 1 helps form the nucleotide binding site, related to Figure 2

(A) Structural comparison of the EM densities corresponding to putative nucleotides observed in VIPP1 maps of three different symmetries (C15, C16, C17; first column from the left) with ADP structural models and cryo-EM densities from known nucleotides. Second column: VIPP1 densities fit with an ADP model. Third and fourth column: VIPP1 densities fit with cryo-EM density from structures of the p97 complex (Banerjee et al., 2016) known to correspond to ADP and ATPγS (black mesh). Notice that the ADP density is a better fit. Fifth and sixth columns: VIPP1 densities displayed at a lower threshold, which grows the occupied volume

(legend continued on next page)

and reveals a small additional density that may correspond to Mg^{2+}. The VIPP1 densities are fit with a structural model of ADP with a Mg^{2+} ion (green sphere). (B) Schematic diagram of the VIPP1 monomer's secondary structure elements (helices H1-H7 in colored rectangles), as shown in Figure 1F. (C) Zoom in on the amino acid sequence spanning H4/5 and H6, diagramming the remodeling of these two helices between layers 1 and 2. (D) Corresponding view of the molecular model, showing the remodeling that occurs between layers 1 and 2. Glu179, which plays a key role in the nucleotide binding pocket, is indicated in magenta. Notice that Glu179 is part of the H4/5 helix in layer 2. However, H4/5 partially opens into a coil in layer 1, placing Glu179 in the loop between the helices as part of the nucleotide binding pocket. (E) Position of ADP between layers 1 and 2 of the VIPP1 ring structure and (F) proposed model for coordination of the nucleotide, Mg^{2+}, and a nucleophilic (nuc) water molecule in the binding pocket. The hypothetical position of the γ phosphate is indicated with (P_i).

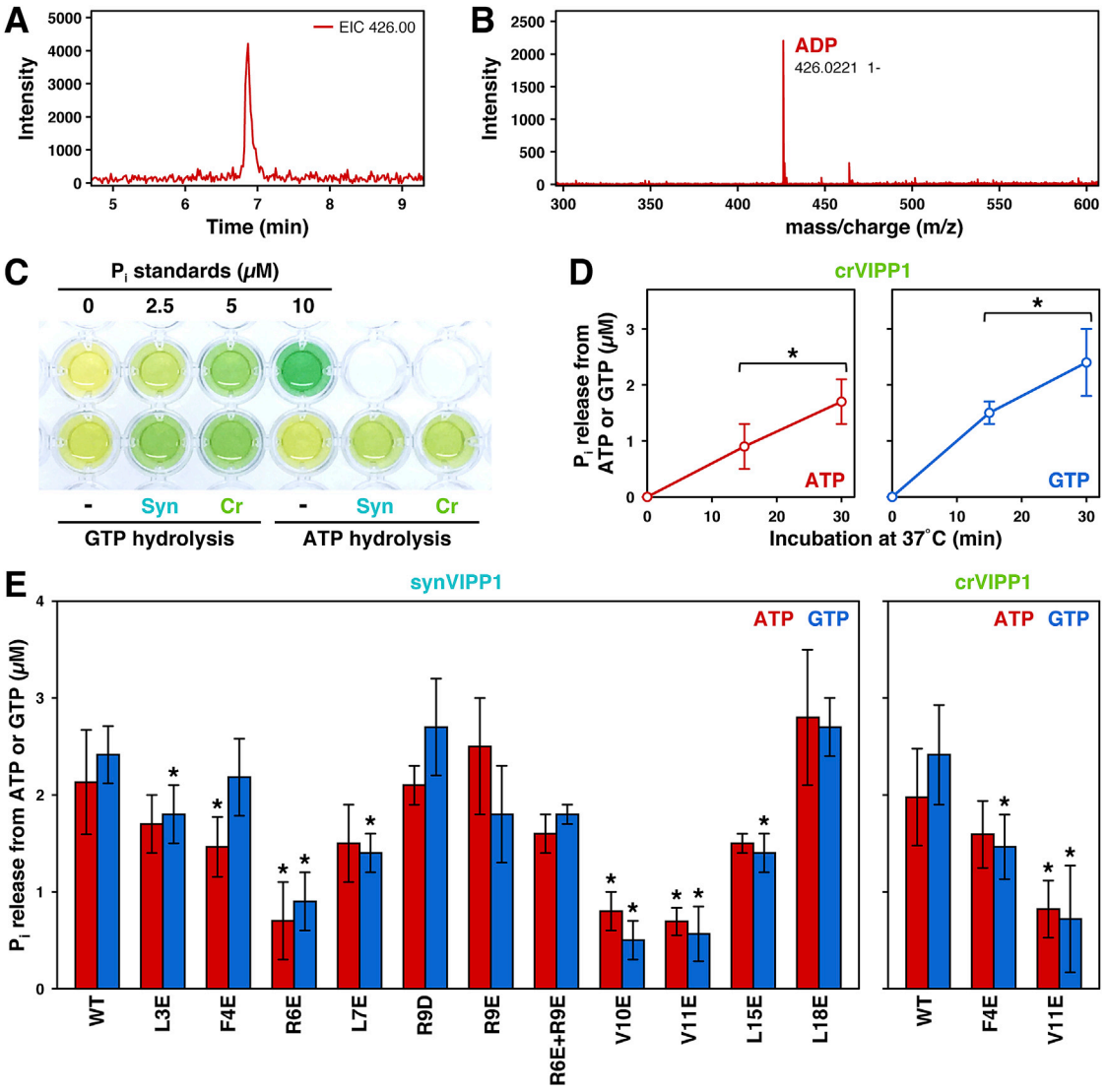

Figure S4. Supplemental mass spectrometry and nucleotide hydrolysis activity data, related to Figure 2

(A and B) RPIP-HPLC profile (A) and subsequent ESI-MS (B) of isolated WT *syn*VIPP1. A distinct mass for ADP was observed. (C) Image of a microwell plate containing an *in vitro* nucleotide hydrolysis assay. Inorganic phosphate (P_i) standards are arrayed in the top row, and the hydrolysis of ATP and GTP by *syn*VIPP1 (Syn) and *cr*VIPP1 (Cr) are assayed on the bottom row (control without protein indicated with "-"). (D) Hydrolysis of ATP and GTP by *cr*VIPP1 is linear as a function of time. Comparable *syn*VIPP1 measurements are shown in Figure 2G. Error bars, standard deviation from 4–5 replicates. Asterisks indicate a significant change between time points (*$p < 0.05$, Welch's t test). (E) *In vitro* ATP and GTP hydrolysis by WT *syn*VIPP1 (left panel) and *cr*VIPP1 (right panel) compared to mutations in the N-terminal H1 helix. Error bars, standard deviation from 3-8 replicates. Asterisks indicate a significant change compared with the WT (*$p < 0.05$, Welch's t test).

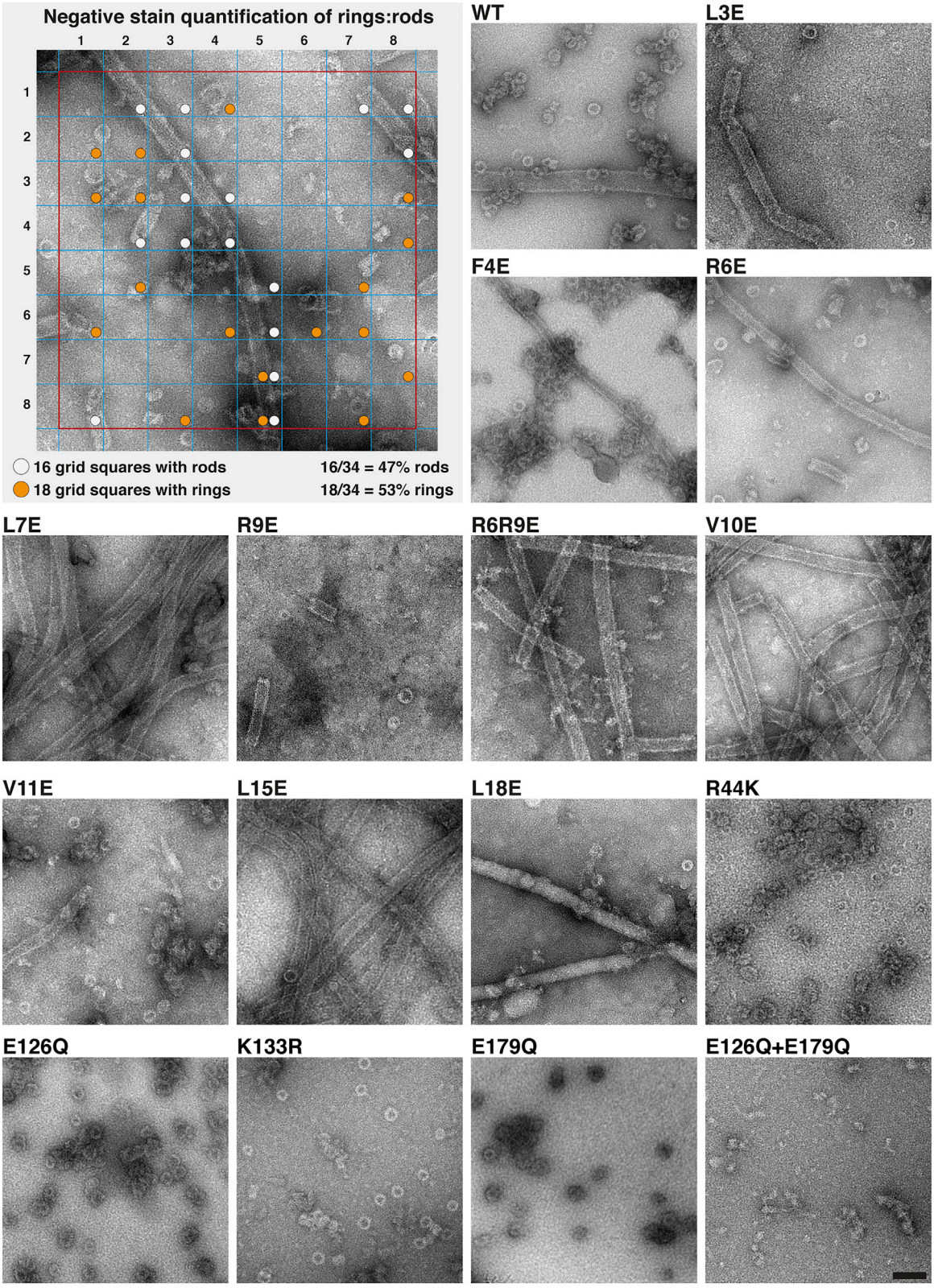

(legend on next page)

Figure S5. Example negative-stain EM images from each *syn*VIPP1 protein, related to Figure 3

Mutant names are indicated above each image. Rods were commonly formed by mutations in the H1 helix (L3E through L18E), whereas mutation of nucleotide pocket residues (R44K through E179Q) yielded WT-like distributions of rings. The E126Q+E179Q double mutant contained abundant small fragments and larger protein aggregates, but no ring or rod structures. Rods were occasionally observed in the WT sample and seemed to be more common at higher protein concentrations. Scale bar: 100 nm. Top Left: Estimation of the percentage of VIPP1 protein assembled into rings versus rods (as plotted in Figure 3F). Negative-stain EM images were overlaid with an 8x8 grid map (grid map border outlined in red; individual grid squares outlined in blue). Grid squares were manually scored for the presence of rings (orange circles) and/or rods (white circles). If more than a quarter of a structure was contained within a grid square, that square was counted. The percentage of VIPP1 oligomerized into rings was roughly estimated by dividing the number of grid squares containing rings by the sum of the squares containing rings and squares containing rods (see calculation below image). For each measurement in Figure 3F, we analyzed 20-50 images from 2-3 grids, produced from 2-4 independent protein preps.

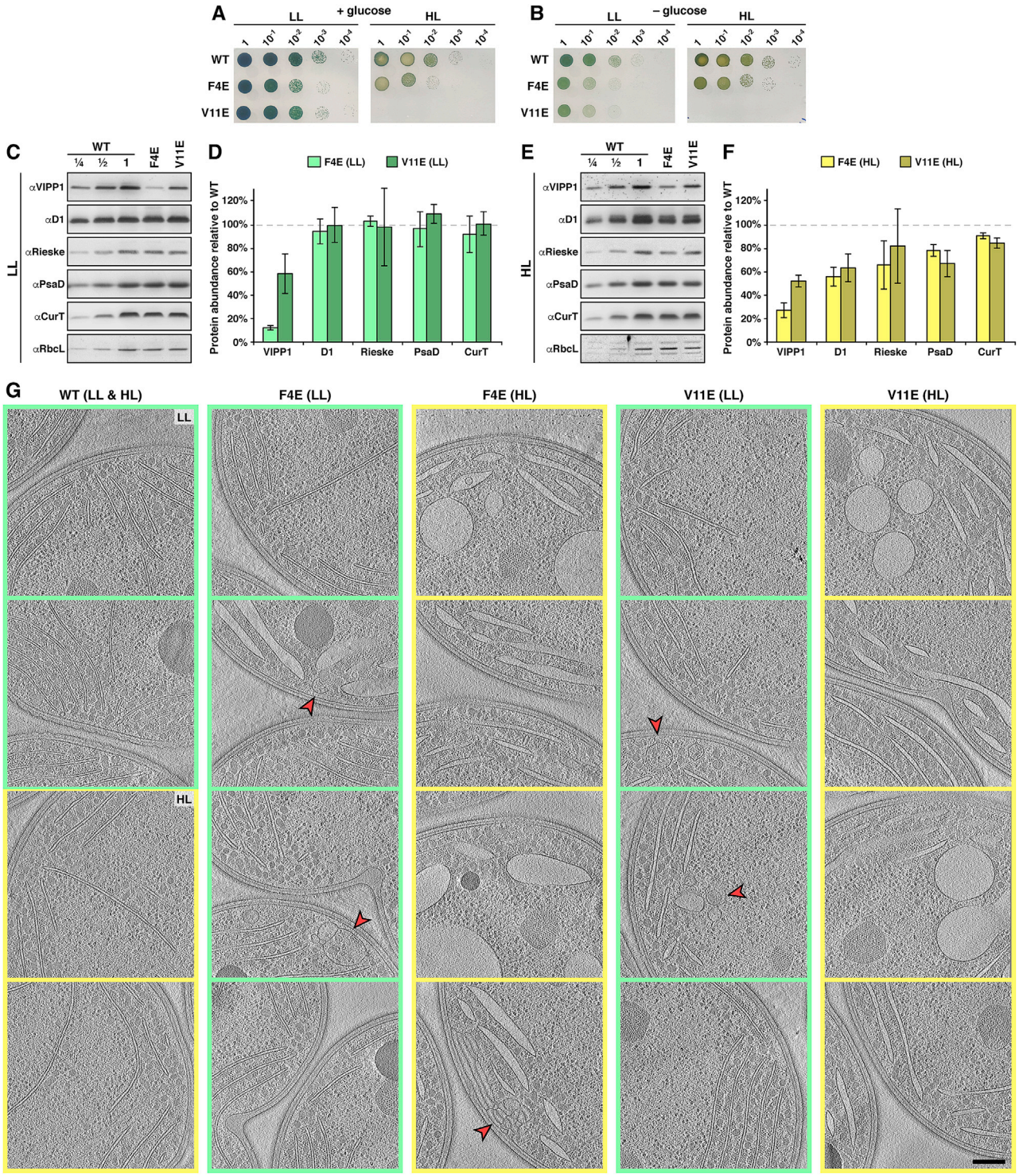

Figure S6. Thylakoid protein levels and *in situ* cryo-ET gallery for the *Synechocystis* H1 mutants, related to Figure 4

(A and B) Spot growth tests of WT control, F4E, and V11E strains after five days on agar plates in low light (LL, 30 μmol photons $m^{-2}s^{-1}$) and high light (HL, 200 μmol photons $m^{-2}s^{-1}$). (A) Cells grown on plates containing glucose. These images are reproduced from Figure 4A but displayed with more natural contrast. (B) Cells grown on plates without glucose. (C and E) Western blot analysis of various thylakoid proteins in WT, F4E, and V11E in LL (C) and after switch to HL for 24 h (E). D1, Rieske, and PsaD are components of photosystem II, cytochrome b_6f, and photosystem I, respectively. The Rubisco large subunit RbcL was used as a

(legend continued on next page)

loading control. (D and F) Relative changes of protein levels in the F4E and V11E mutants compared to WT, quantified from the western blots in C and E. Plots show mean and standard deviation (error bars) from three independent biological replicates. (G) Overviews of additional tomograms from the WT, F4E, and V11E strains grown in LL (green) and after 24 h in HL (yellow). Quantification of luminal widths is shown in Figure 4L. Red arrowheads indicate abnormal convergence zone architecture (more examples in Figure S7). Scale bar: 200 nm.

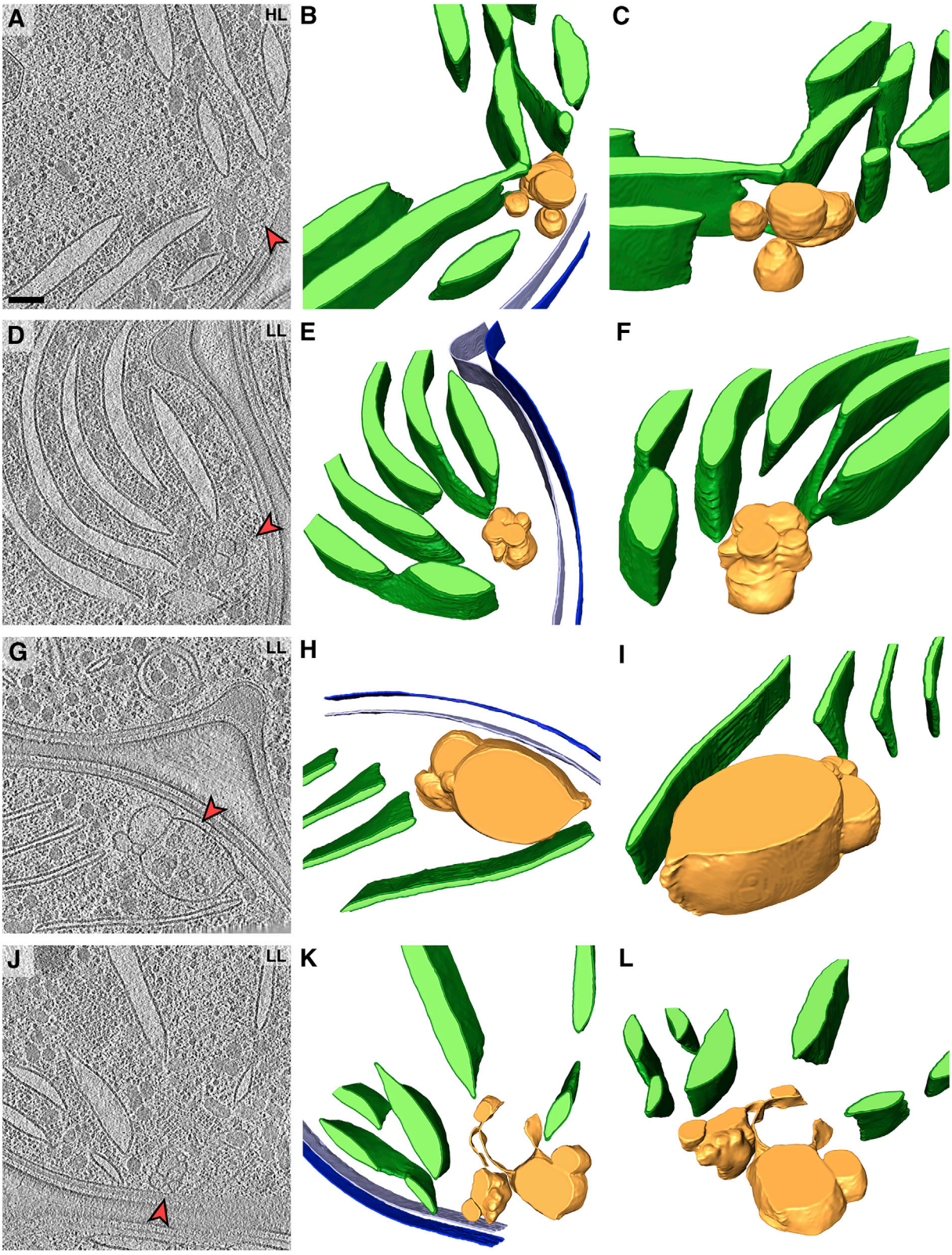

(legend on next page)

Figure S7. Examples of defective convergence zones in the F4E mutant, related to Figure 4

(A, D, G, and J) 2D slices through tomographic volumes. Red arrowheads point to abnormal membranes filled with cytosolic material at convergence zones. HL and LL conditions are indicated. (B, E, H, and K) Top views and (C, F, I, and L) inclined views showing 3D segmentations of the tomograms (dark green, thylakoid membranes; light green, thylakoid lumen; dark blue, outer membrane, light blue, plasma membrane; yellow/gold, defective convergence membranes). (A–C) are additional views of Figure 4G and 4H. For examples in the V11E mutant, see Figure S6. Scale bar: 100 nm.

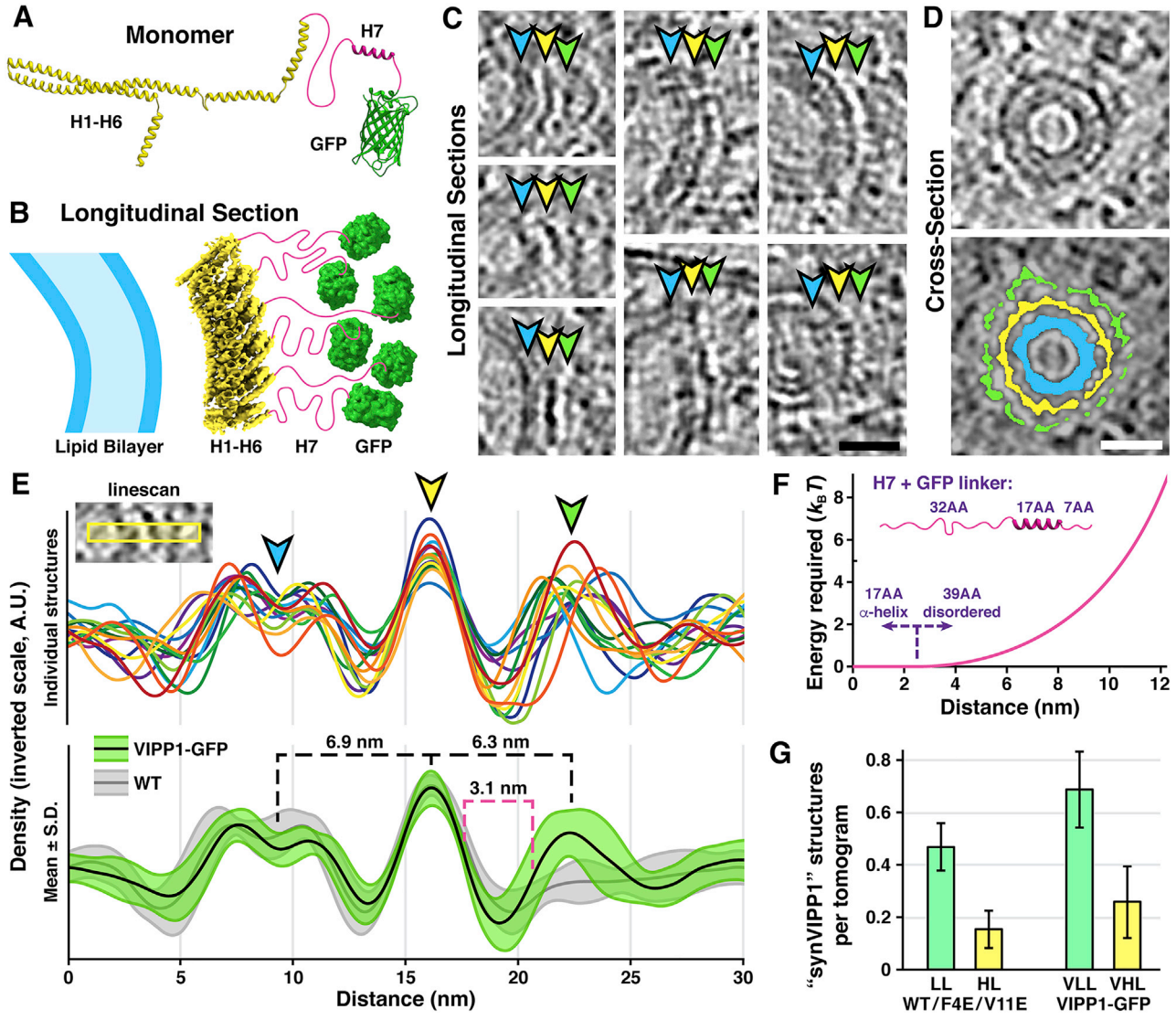

Figure S8. An extra layer of density decorates putative *syn*VIPP1 structures in *Synechocystis* cells expressing VIPP1-GFP, related to Figure 5

(A) Structural diagram of a single VIPP1-GFP monomer (yellow, VIPP1 helices H1-H6; magenta, H7 as well as the disordered domain connecting it to H6 and an additional short linker connecting it to the GFP; green, GFP). (B) Diagram of a longitudinal section through the wall of a VIPP1-GFP ring (colored as in A) encapsulating a membrane (blue). This diagram presents the same perspective as C and E. (C) 2D slices from *in situ* tomograms showing longitudinal slices through the walls of putative *syn*VIPP1-GFP structures. The images show raw unfiltered tomograms, which correspond to the line scan values in E. Arrowhead colors match B (blue, membrane bilayer; yellow, putative VIPP1; green, putative GFP). (D) Cryo-ET cross-section of a putative *syn*VIPP1-GFP structure. Top panel: raw tomogram density, bottom panel: the three layers of density colored according to their identity. Scale bars in C and D: 20 nm. (E) 2D line scan average intensity profiles through the putative *syn*VIPP1-GFP structures, measured as shown in the upper left inset (line scan width: 5.3 nm). Line scans are plotted on an inverted scale (dark densities have high values). Top: measurements of 15 putative *syn*VIPP1-GFP structures. Arrowheads correspond to C. Bottom: mean ± standard deviation for the VIPP1-GFP line scans (black, green) and for line scans of 15 putative *syn*VIPP1 structures from WT cells (gray). Notice the additional peak in cells expressing VIPP1-GFP. Inter-peak distances are indicated with dashed black lines. The average distance between the side of the putative VIPP1 wall and the side of the putative GFP is indicated with a dashed magenta line. (F) The estimated energy required to stretch the magenta linker region (H7 + disordered linkers) a given distance away from the VIPP1 wall (k_B: Boltzmann constant, T: temperature). The H7 helix is modeled as a rigid body spanning 2.55 nm. The 39 total disordered amino acids are modeled according to (He et al., 2020). Based on this calculation, GFP can be positioned up to ~8 nm from the VIPP1 wall with minimal energy cost, easily spanning the average distance of 3.1 nm observed experimentally (magenta line in E). (G) Mean number of putative *syn*VIPP1 structures found per tomogram under different light conditions. Low light (LL): 30 μmol photons $m^{-2}s^{-1}$, high light (HL): 200 μmol photons $m^{-2}s^{-1}$ for 24 h, very low light (VLL): 8 μmol photons $m^{-2}s^{-1}$, very high light (VHL): 600 μmol photons $m^{-2}s^{-1}$ for 1 h. Cumulative of WT, F4E, and V11E strains: n = 68 LL tomograms, 26 HL tomograms; *vipp1-GFP* strain: n = 42 VLL tomograms, 31 VHL tomograms. Error bars, standard error of the mean.